LIMNOLOGY and OCEANOGRAPHY: METHODS

ASLO

Limnol. Oceanogr.: Methods 17, 2019, 377–394

doi: 10.1002/lom3.10320

A blended inherent optical property algorithm for global satellite ocean color observations

Wei Shi [1,2]* **Menghua Wang** [1]

[1]Center for Satellite Applications and Research, National Environmental Satellite, Data, and Information Service, National Oceanic and Atmospheric Administration, College Park, Maryland

[2]Cooperative Institute for Research in the Atmosphere at Colorado State University, Fort Collins, Colorado

Abstract

Water inherent optical properties (IOPs) can be derived from satellite-measured normalized water-leaving radiance ($nL_w(\lambda)$) spectra. In this study, we evaluate the performance of the quasi-analytical algorithm (QAA) and the near-infrared (NIR)-based IOP algorithm using a Hydrolight simulation data set covering a wide range of water types that span from clear open ocean to turbid coastal/inland waters. The NIR-based algorithm produces significantly improved IOP retrievals over turbid coastal and inland waters, while the QAA algorithm performs well in the open ocean and less turbid coastal waters. Based on the advantages of the NIR-based and QAA-based algorithms, a combination of the NIR- and QAA-based algorithm has been proposed using satellite-measured $nL_w(745)$ as the threshold in order to produce accurate IOP products for both the open ocean and turbid coastal/inland waters. The new combined IOP algorithm can produce reasonably accurate IOP data for all water types, and can be easily implemented into the satellite ocean color data processing. The La Plata River Estuary region is used as an example to show the difference in performance of IOP retrievals from the Visible Infrared Imaging Radiometer Suite (VIIRS) measurements between 2012 and 2017 with the NIR-based, QAA-based, and NIR-QAA combined IOP algorithms. We also demonstrate that the NIR-QAA combined algorithm can be applied to VIIRS global ocean color observations to derive good quality IOP products in China's east coastal region, the US east coastal region, and the region of Mississippi River Estuary and tributaries.

Water inherent optical properties (IOPs) are the absorption and scattering of pure water, phytoplankton, color dissolved organic matter (CDOM), minerals, and so on. The normalized water-leaving radiance spectra ($nL_w(\lambda)$) from the satellite ocean color observations are determined by IOPs (Gordon et al. 1988). Correspondingly, IOPs can also be inferred from the $nL_w(\lambda)$ spectra from satellite remote sensing. Retrievals of the water IOPs such as absorption coefficients of the phytoplankton, CDOM, and backscattering coefficients of the phytoplankton and non-algal particles from the satellite ocean color remote sensing for both open oceans and the coastal waters are important to monitoring and assessing marine environments and natural hazards such as the biological impact of hurricanes and blooms of harmful algae. Satellite-derived water IOPs allow the study of the ocean's physical, optical, biological, and biogeochemical processes and their interactions, and permit an evaluation of the ocean's biological and biogeochemical responses to long-term global climate change.

*Correspondence: wei.1.shi@noaa.gov

Most of the current global satellite IOP algorithms for application in ocean color satellites such as the Sea-viewing Wide Field-of-view Sensor (SeaWiFS), the Moderate Resolution Imaging Spectroradiometer (MODIS) on the Terra and Aqua, and the Visible Infrared Imaging Radiometer Suite (VIIRS) on the Suomi national polar-orbiting partnership (SNPP) and NOAA-20 are based on the study of Gordon et al. (1988), which shows that a semi-analytical radiance model can be used to predict the upwelling spectral radiance in visible wavelengths with various materials in the water such as phytoplankton pigment concentration, dissolved organic and detrital matter, and so on. Specifically, the remote-sensing reflectance just beneath the ocean surface $r_{rs}(\lambda)$ can be written as

$$r_{rs}(\lambda) = g_1\left(\frac{b_b(\lambda)}{a_t(\lambda)+b_b(\lambda)}\right) + g_2\left(\frac{b_b(\lambda)}{a_t(\lambda)+b_b(\lambda)}\right)^2 \quad (1)$$

where g_1 and g_2 are 0.0949 and 0.0794 sr^{-1} (Gordon et al. 1988). Coefficients g_1 and g_2 are also tuned and set to be 0.089 and 0.125 sr^{-1} for IOP retrievals with the quasi-analytical algorithm (QAA) (Lee et al. 2002). $a_t(\lambda)$ and $b_b(\lambda)$ are total absorption and backscattering coefficients, respectively. $r_{rs}(\lambda)$ can be computed from the remote-sensing reflectance above the

surface $R_{rs}(\lambda)$ or the normalized water-leaving radiance $nL_w(\lambda)$ (Morel and Gentili 1996; Gordon 2005; Wang 2006). The total absorption coefficient $a_t(\lambda)$ is the sum of the absorption coefficients from pure seawater $a_w(\lambda)$, phytoplankton $a_{ph}(\lambda)$, dissolved matter $a_g(\lambda)$, and nonalgal particles $a_d(\lambda)$. Coefficient $b_b(\lambda)$ is the sum of backscattering coefficients for pure seawater $b_{bw}(\lambda)$ and particulate matter $b_{bp}(\lambda)$.

Specifically, the Garver-Siegel-Maritorena (GSM) IOP algorithm (Garver and Siegel 1997; Maritorena et al. 2002) fixes the absorption for dissolved and detrital matter ($a_{dg}(\lambda)$) slope S to be 0.0206 nm^{-1}, and $b_{bp}(\lambda)$ power law exponential slope η to be 1.0037 in order to apply a nonlinear least-square technique to fit $R_{rs}(\lambda)$ at the four or five wavelengths of the satellite ocean color sensors. On the other hand, the QAA algorithm (Lee et al. 2002) starts with the computation of $a_t(\lambda_0)$ at a green/red wavelength using the empirical formula in Morel and Maritorena (2001). Coefficient $b_b(\lambda_0)$ is then calculated algebraically from $r_{rs}(\lambda)$ (Gordon et al. 1988; Hoge and Lyon 1996; Lee et al. 2002). The $b_{bp}(\lambda)$ power law exponential slope η is estimated from $r_{rs}(\lambda)$ at the blue and green bands with an empirical formula (Lee et al. 2002). Decomposition of $a_t(\lambda)$ into $a_{ph}(\lambda)$ and $a_{dg}(\lambda)$ is carried out with the empirical formula using $a_t(410)$, $a_t(443)$, and $r_{rs}(\lambda)$ at the blue and green bands (Lee et al. 2002). The generalized IOP (GIOP) algorithm (Werdell et al. 2013) is focused on the development of the GIOP model for the construction of different semi-analytical algorithms; thus, users can test different combinations of IOP models. It permits isolation and evaluation of specific modeling assumptions, construction of semi-analytical algorithms, and development of a regionally tuned IOP algorithm. The default configuration for $b_{bp}(\lambda)$ in GIOP is the same as in the QAA algorithm (Lee et al. 2002). Following the configuration of the GIOP algorithm, the retrievals of $b_{bp}(\lambda)$, $a_{ph}(\lambda)$, and $a_{dg}(\lambda)$ can be calculated via the linear or nonlinear least-square inversions of Eq. 1 using the $r_{rs}(\lambda)$ spectra.

It is noted that there are some restrictions for all three IOP algorithms. GSM is generally only valid in the open ocean with a $b_{bp}(443)$ range that is less than ~ 1.0 m^{-1}, and an $a_{dg}(\lambda)$ that is less than ~ 2.0 m^{-1} (Garver and Siegel 1997; IOCCG 2006). QAA and GIOP algorithms are only applicable to the open ocean and less-turbid coastal waters because both of these algorithms only use the $r_{rs}(\lambda)$ in the blue and green/red bands to estimate the $b_{bp}(\lambda_0)$ and $b_{bp}(\lambda)$ power law exponential slope η with the empirical formulas (Lee et al. 2002; Werdell et al. 2013). In turbid and highly turbid waters, studies have shown that $r_{rs}(\lambda)$ loses its sensitivity with the change of suspended particles in the visible wavelengths (Shi and Wang 2009*a*, 2014; Shen et al. 2010*a*). Thus, it is necessary to retrieve ocean biological and biogeochemical properties such as chlorophyll *a* (Chl *a*) concentration, water turbidity, total suspended matter (TSM), and so on, with the satellite measurements in the near-infrared (NIR) wavelengths (Gitelson et al. 2007; Dogliotti et al. 2015; Shi et al. 2018).

Most of satellite ocean color products are derived from $nL_w(\lambda)$ spectra in the visible wavelengths. Unlike open oceans, coastal and inland water regions, particularly highly turbid regions like river estuaries, are dominated with inorganic materials such as clays, silts, and fine sands from the bottom or from the river flows (Bowers and Binding 2006). Suspended particles in coastal and estuarine waters are commonly in the form of aggregates or flocs (Eisma et al. 1990). For the open ocean, satellite-measured $nL_w(\lambda)$ spectra can be generally retrieved with uncertainty of ~ 5% at the blue band; therefore, Chl *a* uncertainty is within ~ 30% (Mcclain et al. 2004; Mcclain 2009). However, there are still some challenges in coastal regions, especially for highly turbid coastal and inland water regions. Such challenges include deriving accurate $nL_w(\lambda)$ spectra, i.e., atmospheric correction (Gordon and Wang 1994; Wang 2007; IOCCG 2010), Chl *a* concentration (O'Reilly et al. 1998; Hu et al. 2012; Wang and Son 2016), $K_d(490)$ (Wang et al. 2009), and the ocean's IOPs (Garver and Siegel 1997; Lee et al. 2002; Werdell et al. 2013). These challenges make it difficult to characterize and assess the physical, biological, and biogeochemical changes with satellite ocean color observations in coastal and inland water regions.

The normalized water-leaving radiance $nL_w(\lambda)$ spectra in the red, NIR, and shortwave infrared (SWIR) wavelengths can only be rarely used in the open ocean to derive ocean's biological and biogeochemical products. However, coastal and inland waters are generally featured with enhanced $nL_w(\lambda)$ at the NIR and SWIR wavelengths. As an example, the NIR ocean reflectance spectral shape represented by the ratio of $nL_w(\lambda)$ at the two NIR bands is highly dynamic and region-dependent (Doron et al. 2011; Shi and Wang 2014). The NIR spectral reflectance feature in the estuary of the Yellow River and Ancient Yellow River is found to be notably different from that of the Yangtze River (Shi and Wang 2014). This makes the satellite ocean color measurements at the red, NIR, and SWIR bands extremely valuable in conducting atmospheric correction (Gordon and Wang 1994; Wang 2007; Wang and Shi 2007), which characterizes and quantifies water properties in coastal and inland waters such as Chl *a* concentration (Gitelson et al. 2007), floating green algae blooms (Hu 2009; Shi and Wang 2009*b*), river plumes (Shi and Wang 2009*c*), TSM (Miller and Mckee 2004; Shen et al. 2010*b*; Son and Wang 2012; Shi et al. 2018), and the light diffuse attenuation coefficient at 490 nm (Wang et al. 2009; Zhang et al. 2012). It is also found that the spectral features of $nL_w(\lambda)$ at the red and NIR wavelengths are dynamic and regional dependent (Ruddick et al. 2006; Doron et al. 2011; Shi and Wang 2014). This can be attributed to the TSM concentrations, suspended particle shapes, size distributions, and compositions of the suspended particles (Stramski et al. 2007; Kostadinov et al. 2009; Shi and Wang 2017).

Based on the fact that, in coastal and inland waters, the absorption coefficient of seawater $a_w(\lambda)$ is the dominant constituent of $a_t(\lambda)$ at the NIR wavelengths; the semi-analytical radiance model as shown in Eq. 1 can be significantly simplified, thereby $b_b(\lambda)$ at the NIR wavelengths can be analytically calculated. Consequently, $b_{bp}(\lambda)$ in the visible wavelengths can be derived from $b_{bp}(\lambda)$ retrievals at the NIR wavelengths (Shi and Wang 2017). Hydrolight simulations show that $b_{bp}(\lambda)$ retrievals are accurate and robust for a wide range of both moderately and highly turbid

waters in comparison to the Hydrolight input $b_{bp}(\lambda)$. In addition, Shi and Wang (2017) demonstrated that the NIR-based $b_{bp}(\lambda)$ algorithm can be applied to VIIRS-SNPP observations to produce $b_{bp}(\lambda)$ products in the global highly turbid waters such as the Bohai Sea and Yellow Sea in China's east coastal region, Amazon River Estuary, and Mississippi River Estuary and tributaries (Shi and Wang 2017).

In this study, we further extend our research to exploit VIIRS-derived $nL_w(\lambda)$ at the visible and NIR bands using the NIR-SWIR combined atmospheric correction algorithm (Wang and Shi 2007) with VIIRS-SNPP observations between 2012 and 2017 to compute the total absorption coefficient $a_t(\lambda)$, color dissolved and detrital absorption coeffficent $a_{dg}(\lambda)$, and phytoplankton absorption coefficent $a_{ph}(\lambda)$ for the global ocean. A scheme is proposed to combine these NIR-based and QAA-based IOP algorithms in order to produce global IOP products from VIIRS-SNPP observations. The advantage of this scheme is first evaluated with Hydrolight simulation data. We demonstrate that this combined IOP algorithm can significantly improve IOP products in coastal and inland waters, and produce high-quality IOP products for both clear open oceans and turbid coastal/inland waters.

Methods

The data set of IOP and $nL_w(\lambda)$ spectra from Hydrolight simulations

Due to the insufficient amount of in situ IOP data and $nL_w(\lambda)$ measurements covering a wide range of IOPs for both the open ocean and turbid coastal/inland water regions, Hydrolight simulations (Mobley et al. 1993; Mobley and Sundman 2013) were conducted to create the data set of IOPs and $nL_w(\lambda)$ spectra for a variety of water types. The Hydrolight radiative transfer model computes radiance distributions and related quantities (e.g., irradiances, reflectance, diffuse attenuation functions, etc.) in various water types using the absorption and backscattering of various constituents in the water, for given bottom depth, IOP property profiles, and atmosphere condition (Mobley et al. 1993).

To generate a representative IOPs and $nL_w(\lambda)$ spectra data set for the global ocean, IOPs from the International Ocean Colour Coordinating Group (IOCCG) synthesized data set for IOP algorithm development in IOCCG Report 5 (IOCCG 2006) were used as the baseline IOPs for the Hydrolight simulations. The IOPs and corresponding apparent optical properties (AOPs) can generally be used to develop, test, evaluate, and compare the IOP and AOP algorithms for satellite ocean color remote sensing. This data set contains 500 records of respective phytoplankton absorptions $a_{ph}(\lambda)$, dissolved matter absorptions $a_g(\lambda)$, nonalgal detrital absorptions $a_d(\lambda)$, and particle backscattering coefficients $b_{bp}(\lambda)$ at the wavelength interval of 10 nm between 400 and 800 nm in addition to the corresponding $R_{rs}(\lambda)$ spectra. However, the data set only covers the water types in the open ocean and less turbid coastal waters.

In order to develop an IOP algorithm for all water types, i.e., clear open ocean waters, less turbid and turbid coastal waters, estuarine, and inland waters, we further expanded the IOCCG simulated data set. Since turbid coastal waters feature enhanced particle backscattering coefficients $b_{bp}(\lambda)$, phytoplankton absorption coefficients $a_{ph}(\lambda)$, and dissolved and detrital matter absorptions $a_{dg}(\lambda)$, the last 25 records of IOPs in the IOCCG data set are chosen first. These 25 records have the highest values in $b_{bp}(\lambda)$, $a_d(\lambda)$, $a_g(\lambda)$, and $a_{ph}(\lambda)$ in the data set. With the assumption that nonalgal detrital backscattering $b_{bd}(\lambda)$ and $a_d(\lambda)$ are proportional to the detritus/mineral concentrations, and $a_g(\lambda)$ and $a_{ph}(\lambda)$ are proportional to the concentrations of the corresponding constituents, we boost detritus/mineral concentrations, $a_g(\lambda)$ and $a_{ph}(\lambda)$, by factors of 1, 2, 5, and 10 times. Thus, the total number of the possible IOP combinations can be as high $25 \times 4 \times 4 \times 4 = 1600$. Of the possible records of IOP data set, we randomly select a certain number of the records as the Hydrolight inputs to generate $nL_w(\lambda)$ spectra for the coastal and inland waters. These enhanced $b_{bp}(\lambda)$, $a_{dg}(\lambda)$, and $a_{ph}(\lambda)$ as well as the corresponding $nL_w(\lambda)$ spectra are randomly selected as the new IOP and $nL_w(\lambda)$ records for turbid coastal and inland waters.

In addition to the new IOP data records, we also ran Hydrolight simulations for the 500 records of IOPs in the synthesized data set from IOCCG Report 5 in order to produce $nL_w(\lambda)$ spectra at the VIIRS-SNPP bands of 410, 443, 486, 551, 671, 745, and 862 nm because the NIR $nL_w(862)$ is not covered in the IOCCG synthesized data set (IOCCG 2006). It has been verified that $nL_w(\lambda)$ spectra from the Hydrolight simulations are consistent with those in the IOCCG synthesized data set.

Hydrolight simulations can be used to build realistic records of enhanced IOPs and the corresponding $nL_w(\lambda)$ spectra in turbid waters with this scheme. Thus, the 500 records of IOPs and Hydrolight-simulated $nL_w(\lambda)$ spectra at the VIIRS wavelengths are combined with those of the enhanced $b_{bp}(\lambda)$, $a_{dg}(\lambda)$, and $a_{ph}(\lambda)$ along with the corresponding Hydrolight-simulated $nL_w(\lambda)$ spectra at the VIIRS bands, building a comprehensive data record of IOPs and $nL_w(\lambda)$ spectra. The new data set covers a variety of water types such as clear open ocean, less-turbid, turbid, and highly turbid coastal and inland waters. Therefore, this new data set can be used to evaluate the performance of various IOP algorithms, and develop a new IOP algorithm for producing good quality IOP products from VIIRS observations.

VIIRS-derived $nL_w(\lambda)$ spectra from the NIR-SWIR based ocean color data processing

VIIRS is one of the major sensors onboard the SNPP satellite, which was launched on 28 October 2011. It has 22 spectral bands, including 14 reflective solar bands, 7 thermal emissive bands, and a panchromatic day/night band. The spectral band specifications are similar to MODIS in order to observe Earth's atmosphere, land, and ocean properties (Goldberg et al. 2013). Ocean color environmental data records are one of the key product suites derived from VIIRS (Wang et al. 2013, 2016).

VIIRS-SNPP has five visible bands (M1–M5) with nominal central wavelengths at 410, 443, 486, 551, and 671 nm, two NIR bands (M6 and M7) at wavelengths of 745 and 862 nm,

and three SWIR bands (M8, M10, and M11) at wavelengths of 1238, 1601, and 2257 nm for satellite ocean color data processing. The spatial resolution of these spectral bands is 750 m. In addition, there are imaging bands (I-bands) with spatial resolution of 375 m. In particular, VIIRS I1 band at 638 nm is useful for various coastal and inland water applications (Wang and Jiang 2018). For satellite ocean color data processing, we also carried out the on-orbit vicarious calibration for VIIRS using the in situ $nL_w(\lambda)$ spectra from the Marine Optical Buoy (MOBY) (Clark et al. 1997) located in the waters off Hawaii (Wang et al. 2016).

To derive $nL_w(\lambda)$ spectra from satellite observations, one fundamental assumption for atmospheric correction is the black ocean assumption at the NIR and SWIR wavelengths for the specific water types. For the open ocean, atmospheric correction can be carried out using the two VIIRS NIR bands (745 and 862 nm) to derive $nL_w(\lambda)$ spectra (Gordon and Wang 1994), and consequently, ocean biological and biogeochemical property data can be obtained using $nL_w(\lambda)$ spectra. For turbid coastal and inland waters, however, $nL_w(\lambda)$ spectra from the visible to NIR wavelengths can be derived using the SWIR-based atmospheric correction algorithm (Wang 2007; Wang and Shi 2007) because the black ocean assumption is generally true for the SWIR bands (Shi and Wang 2009*a*), e.g., at the VIIRS SWIR bands of 1238, 1601, and 2257 nm.

VIIRS ocean color products are produced with the official NOAA VIIRS ocean color data processing system, i.e., the multisensor level-1 to level-2 (MSL12) (Wang et al. 2013, 2014). A method of ocean color data processing using the combined NIR and SWIR bands for atmospheric correction for satellite ocean color data processing (Wang and Shi 2007) was implemented in the MSL12 ocean color data processing system. With the NIR-SWIR combined atmospheric correction algorithm, ocean color data can be processed using the standard (NIR) atmospheric correction algorithm for the open ocean (Gordon and Wang 1994), whereas for the turbid coastal and inland waters, the SWIR atmospheric correction algorithm (Wang 2007) can be executed. The combined NIR-SWIR algorithm has been used to routinely produce global $nL_w(\lambda)$ spectra for VIIRS satellite ocean color data processing. In this study, $nL_w(\lambda)$ spectra derived from the NIR-SWIR atmospheric correction algorithm are used to evaluate and demonstrate IOP products with different IOP algorithms for a variety of ocean regions such as China's east coastal region, the La Plata River Estuary, and the Mississippi River Estuary region.

The QAA-based and NIR-based IOP algorithms

The QAA IOP algorithm was developed to derive the IOPs for optically deep waters (Lee et al. 2002). Briefly, the QAA algorithm includes two steps. The first step is to derive the total absorption coefficients $a_t(\lambda)$ and particle backscattering coefficients $b_{bp}(\lambda)$. An empirical formula is used to compute $a_t(\lambda)$ at the green/red wavelengths from $R_{rs}(\lambda)$ in the visible bands (Morel and Maritorena 2001). It is then applied to the water-leaving reflectance model to calculate $b_{bp}(\lambda_0)$ at the green/red wavelengths. The power law exponential slope η is also empirically estimated from $R_{rs}(\lambda)$ in the visible bands. With $b_{bp}(\lambda_0)$ at the green/red wavelengths and the power law exponential slopes η, $b_{bp}(\lambda)$ spectra are consequently derived, and they are applied to the remote-sensing reflectance model to derive $a_t(\lambda)$ spectra.

The purpose of the second step in the QAA algorithm is to decompose $a_t(\lambda)$ into the dissolved and detrital absorption coefficient, $a_{dg}(\lambda)$, and the phytoplankton absorption coefficient, $a_{ph}(\lambda)$. In this step, the spectral ratio of $a_{ph}(410)/a_{ph}(443)$ is first estimated, and next the spectral slope S of $a_{dg}(\lambda)$ is calculated. These two parameters are both based on the empirical formulas from the in situ observations. With the known $a_{ph}(410)/a_{ph}(443)$, S, $a_t(410)$, and $a_t(443)$ from step 1, $a_{dg}(443)$ and $a_{ph}(443)$ can be computed accordingly. Using $a_{dg}(443)$ and spectral slope S of $a_{dg}(\lambda)$, $a_{dg}(\lambda)$ spectra can be derived. Thus, $a_{ph}(\lambda)$ is consequently computed after deducting $a_{dg}(\lambda)$ and $a_w(\lambda)$ from $a_t(\lambda)$.

In comparison to the QAA IOP algorithm, Shi and Wang (2014, 2017) show that $b_{bp}(\lambda)$ can be computed analytically in turbid coastal and inland waters with the NIR-based $b_{bp}(\lambda)$ algorithm from VIIRS-SNPP observations. Briefly, the pure seawater absorption coefficients $a_w(\lambda)$ at the NIR bands are typically significantly higher than those from other constituents, i.e., $a_w(\lambda) >> a_{ph}(\lambda)$, $a_g(\lambda)$, and $a_d(\lambda)$. For example, $a_w(862)$ is ~ 5 m^{-1}, while $a_{ph}(\lambda)$, $a_g(\lambda)$, and $a_d(\lambda)$ at the NIR 862 nm are normally negligible compared to $a_w(862)$. Therefore, with the spectral features of $a_w(\lambda)$, $a_{ph}(\lambda)$, $a_g(\lambda)$, and $a_d(\lambda)$ at the VIIRS NIR 745 and 862 nm bands, $b_b(\lambda)/(a(\lambda) + b_b(\lambda))$ can be approximated as

$$\left(\frac{b_b(\lambda)}{a(\lambda)+b_b(\lambda)}\right) \approx \left(\frac{b_b(\lambda)}{a_w(\lambda)+b_b(\lambda)}\right). \quad (2)$$

The NIR-based $b_{bp}(\lambda)$ algorithm is robust, and can be used to derive $b_{bp}(\lambda)$ for turbid waters when $nL_w(745)$ and $nL_w(862)$ are less than ~ 6 mW cm^{-2} μm^{-1} sr^{-1} and ~ 4 mW cm^{-2} μm^{-1} sr^{-1} (Shi and Wang 2017), respectively. After deriving $b_{bp}(\lambda)$ in the turbid waters, $a_t(\lambda)$ spectra can be computed with the IOP-reflectance model as shown in Eq. 1. Following the same approach in the QAA algorithm, $a_t(\lambda)$ can be further decomposed into the dissolved and detrital absorption coefficient $a_{dg}(\lambda)$ and phytoplankton absorption coefficient $a_{ph}(\lambda)$ in turbid waters. Table 1 summarizes differences between the NIR-based and QAA-based IOP algorithms.

In this study, we evaluate and compare the performance of the NIR-based and QAA-based IOP retrievals using the new Hydrolight-generated comprehensive data set of IOPs and the corresponding $nL_w(\lambda)$ spectra. Since this data set covers various water types from clear open ocean waters, coastal less-turbid waters, and coastal, estuarine, and inland turbid and highly turbid waters, this evaluation can help to understand the performance of these two IOP algorithms when they are used to produce IOP products from VIIRS global ocean color observations.

In addition, a previous study revealed the advantages and disadvantages of the QAA-based and NIR-based $b_{bp}(\lambda)$

algorithms (Shi and Wang 2017). These two $b_{bp}(\lambda)$ algorithms actually can be complementary with each other. Thus, a combined NIR- and QAA-based $b_{bp}(\lambda)$ algorithm was proposed and demonstrated an improvement of global $b_{bp}(\lambda)$ for both open oceans and coastal turbid waters (Shi and Wang 2017). In this study, we further explore the possibility for a combined algorithm for all IOP products including $a_{ph}(\lambda)$, $a_{dg}(\lambda)$, and $a_t(\lambda)$ in order to produce high-quality IOP products from VIIRS global ocean observations. Specifically, the IOP products derived from the combined NIR- and QAA-based algorithm will be demonstrated in various regions.

Development of the combined IOP algorithm with the Hydrolight simulation data set

The new comprehensive Hydrolight simulation data set is used to evaluate the performance of the NIR-based, QAA-based, and NIR-QAA combined IOP algorithms. The total number of records for IOPs and $nL_w(\lambda)$ is 664. Figure 1 shows the comparisons of the NIR-derived $b_{bp}(\lambda)$ vs. known $b_{bp}(\lambda)$ (Fig. 1a), the NIR-derived $a_{ph}(\lambda)$ vs. known $a_{ph}(\lambda)$ (Fig. 1b), the NIR-derived $a_{dg}(\lambda)$ vs. known $a_{dg}(\lambda)$ (Fig. 1c), and the NIR-derived $a_t(\lambda)$ vs. known $a_t(\lambda)$ (Fig. 1d). High uncertainties of the NIR-based $b_{bp}(\lambda)$ (Fig. 1a) and $a_t(\lambda)$ (Fig. 1d) occur for the clear open ocean waters with known $b_{bp}(\lambda) < 0.02$–0.03 m^{-1} and $a_t(\lambda) < 0.1$ m^{-1}, respectively. This is attributed to the extremely low $nL_w(\lambda)$ at the VIIRS NIR bands for the open ocean waters. On the other hand, the NIR-based IOP algorithm for $b_{bp}(\lambda)$ and $a_t(\lambda)$ shows high level of accuracy for high $b_{bp}(\lambda)$ and $a_t(\lambda)$ values as shown in Fig. 1a,d.

Figure 1b,c shows that the uncertainties of $a_{dg}(\lambda)$ and $a_{ph}(\lambda)$ are high for low $a_{dg}(\lambda)$ and $a_{ph}(\lambda)$, while the performance of the NIR-based $a_{dg}(\lambda)$ and $a_{ph}(\lambda)$ in coastal turbid waters with high $a_{dg}(\lambda)$ and $a_{ph}(\lambda)$ values is reasonably good. This demonstrates that the NIR-based IOP algorithm for $b_{bp}(\lambda)$, $a_t(\lambda)$, $a_{dg}(\lambda)$, and $a_{ph}(\lambda)$ can be used to derive IOPs for coastal turbid waters with good accuracy, but it may lead to significant biases and uncertainties in clear open ocean waters.

Figure 2 shows the performance of the $b_{bp}(\lambda)$ (Fig. 2a), $a_{ph}(\lambda)$ (Fig. 2b), $a_{dg}(\lambda)$ (Fig. 2c), and $a_t(\lambda)$ (Fig. 2d) derived from $nL_w(\lambda)$ spectra with the QAA IOP algorithm in comparison to the Hydrolight IOP inputs. Figure 2a shows that the QAA-based $b_{bp}(\lambda)$ performs well for $b_{bp}(\lambda) < 0.1$ m^{-1}. However, the QAA-based $b_{bp}(\lambda)$ is significantly underestimated for $b_{bp}(\lambda)$ approximately greater than 0.2–0.3 m^{-1}.

The uncertainty results in Figs. 1, 2 are consistent with the findings in Lee et al. (2010). Figure 1 indeed shows that uncertainties of $a_{ph}(\lambda)$ are larger than those of $a_{dg}(\lambda)$ when $a_{ph}(\lambda)$ and $a_{dg}(\lambda)$ are similar, even though $a_t(\lambda)$ retrievals agree well with $a_t(\lambda)$ input in the range of $a_t(\lambda)$ approximately greater than 0.5 m^{-1}. Figure 2 also shows that $a_t(\lambda)$ retrievals in the blue-green wavelengths are generally within ~ 10% for 500 records of the IOCCG data set. It shows that uncertainties of $a_{ph}(\lambda)$ are larger than those of $a_{dg}(\lambda)$ for 500 records of the IOCCG data set.

Similarly, $a_t(\lambda)$ retrievals are generally consistent with the input $a_t(\lambda) < 1.0$ m^{-1} (Fig. 2d), but significant underestimations can be found with increasing $a_t(\lambda)$. It performs better than $a_{ph}(\lambda)$ and $a_{dg}(\lambda)$, but notable uncertainties and biases still exist especially in the range of $a_t(\lambda)$ approximately greater than 1.0 m^{-1}. The QAA $a_{ph}(\lambda)$ retrievals (Fig. 2b) show that the QAA algorithm performed better with low $a_{ph}(\lambda)$ than those with high $a_{ph}(\lambda)$ (Fig. 2b). In fact, Fig. 2 shows that the QAA-derived $a_{ph}(\lambda)$ tends to be underestimated when $a_{ph}(\lambda)$ is greater than 0.5 m^{-1}. Similarly, $a_{dg}(\lambda)$ retrievals are also underestimated when $a_{dg}(\lambda)$ greater than 3 m^{-1} (Fig. 2c). In fact, the simulation performance evaluation for the QAA IOP algorithm shows that the QAA-based IOP algorithm is not suitable for turbid coastal waters, which normally feature high values of $b_{bp}(\lambda)$, $a_t(\lambda)$, $a_{dg}(\lambda)$, and $a_{ph}(\lambda)$.

Some of the different and complementary performances of the QAA-based and NIR-based IOP algorithms for various water types as shown in Figs. 1, 2 suggest that a combined IOP algorithm is necessary in order to produce high-quality IOP products for both open oceans and turbid coastal/inland waters. In fact, it has been demonstrated that the approach of the NIR-SWIR atmospheric correction algorithm can combine the NIR- and SWIR-based atmospheric correction algorithms in order to derive high-quality $nL_w(\lambda)$ spectra for the open

Table 1. Comparison between QAA-based and NIR-based IOP algorithms.

Parameter	QAA v5 IOP algorithm	NIR-based IOP algorithm
$R_{rs}(\lambda)$ $r_{rs}(\lambda)$ conversion	$r_{rs}(\lambda) = R_{rs}(\lambda)/(0.52 + 1.7R_{rs}(\lambda))$	Same in QAA
$u(\lambda) = b_b(\lambda)/(a(\lambda) + b_b(\lambda))$	$u(\lambda) = \frac{-g_0 + \sqrt{g_0^2 + 4g_1 r_{rs}(\lambda)}}{2g_1}$ $g_0 = 0.089$, $g_1 = 0.125$	$u(\lambda) = \frac{-g_0 + \sqrt{g_0^2 + 4g_1 r_{rs}(\lambda)}}{2g_1}$ $g_0 = 0.0949$, $g_1 = 0.0794$
Reference IOP parameter	$\chi = \log\left(\frac{r_{rs}(443) + r_{rs}(486)}{r_{rs}(\lambda_0) + 5r_{rs}(671)\frac{r_{rs}(671)}{r_{rs}(486)}}\right)$	$b_b(\lambda_0) \approx \frac{a_w(\lambda_0)u(\lambda_0)}{1-u(\lambda_0)}$ λ_0 = 745 or 862 nm
	$a(\lambda_0) = a_w(\lambda_0) + 10^{-1.146 - 1.366\chi - 0.469\chi^2}$	
	$b_b(\lambda_0) = \frac{a(\lambda_0)u(\lambda_0)}{1-u(\lambda_0)}$ $\lambda_0 = 551$ nm	
$b_{bp}(\lambda)$ spectral relation	$b_{bp}(\lambda) = b_{bp}(\lambda_0)\left(\frac{\lambda_0}{\lambda}\right)^{\eta}$ $\lambda_0 = 551$ nm	$b_{bp}(\lambda) = b_{bp}(\lambda_0)\left(\frac{\lambda_0}{\lambda}\right)^{\eta}$ $\lambda_0 = 746$ or 862 nm
$b_{bp}(\lambda)$ power law slope	$\eta = 2.0\left(1 - 1.2\exp\left(-0.9\frac{r_{rs}(443)}{r_{rs}(551)}\right)\right)$	$\eta = \log\left(\frac{b_{bp}(862)}{b_{bp}(745)}\right) / \log\left(\frac{745}{862}\right)$
ζ : $a_{ph}(410)/a_{ph}(443)$	$\zeta = 0.74 + \frac{0.2}{0.8 + r_{rs}(443)/r_{rs}(551)}$	Same in QAA
ξ : $a_{dg}(410)/a_{dg}(443)$	$\xi = e^{S(443 - 410)}$	Same in QAA
	$S = 0.015 + \frac{0.002}{0.6 + r_{rs}(443)/r_{rs}(551)}$	

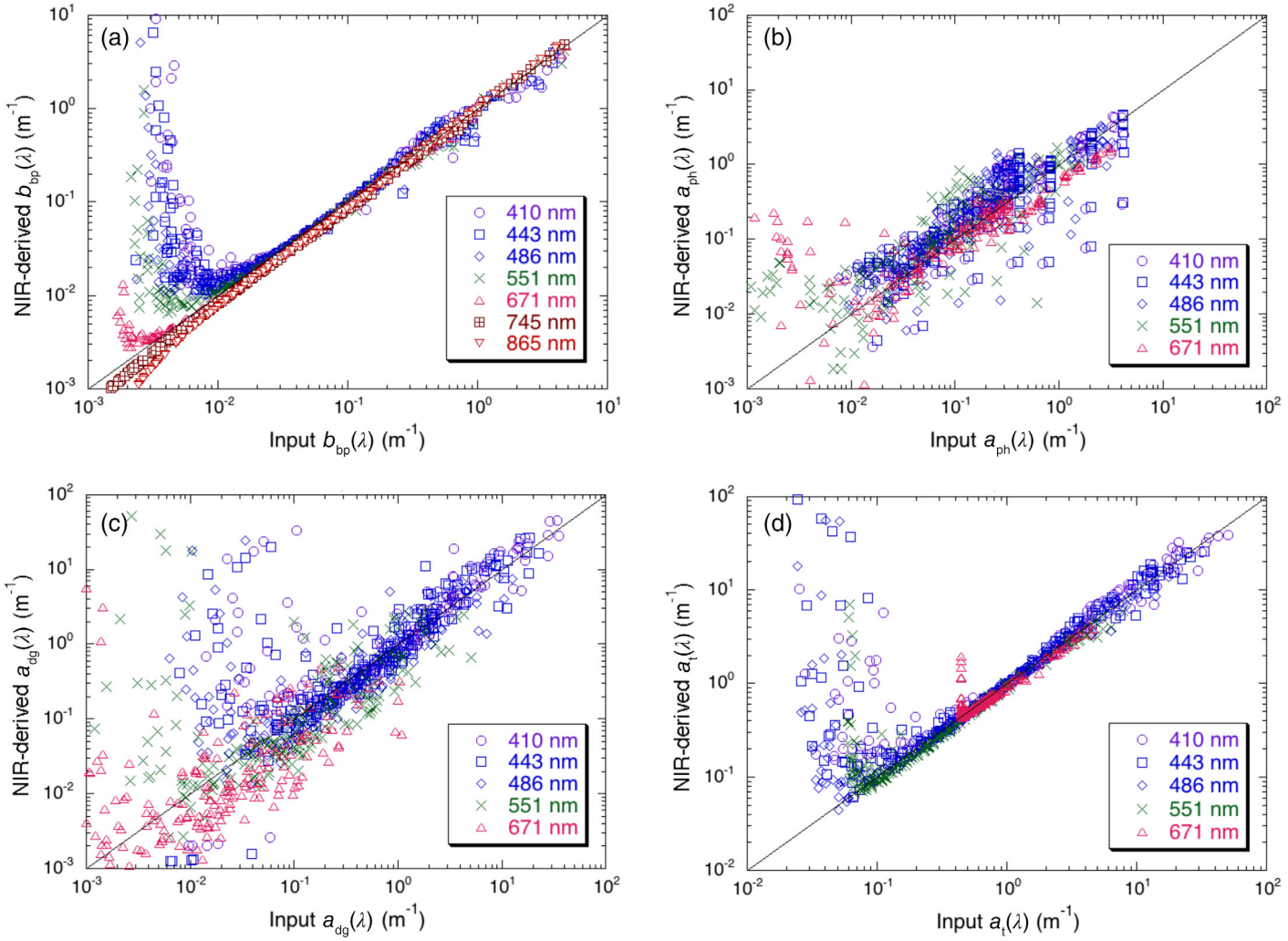

Fig. 1. Comparison of the NIR-based IOP retrievals with Hydrolight inputs (true values) at VIIRS spectral bands for (**a**) $b_{bp}(\lambda)$, (**b**) $a_{ph}(\lambda)$, (**c**) $a_{dg}(\lambda)$, and (**d**) $a_t(\lambda)$.

ocean and turbid coastal/inland waters (Wang and Shi 2007). Similarly, a method was proposed for the combined NIR- and QAA-based $b_{bp}(\lambda)$ algorithm using $nL_w(745)$ as the criteria to determine which algorithm should be used for producing VIIRS $b_{bp}(\lambda)$ data (Shi and Wang 2017).

Following the same strategy, a combined scheme is developed and proposed to derive all IOPs, i.e., $b_{bp}(\lambda)$, $a_{ph}(\lambda)$, $a_{dg}(\lambda)$, and $a_t(\lambda)$ in order to produce accurate IOP products for both open ocean and turbid coastal/inland waters. This scheme can be easily implemented into the MSL12 ocean color data processing system. With extensive tests and evaluations, the specific procedure for the NIR-QAA IOP scheme is outlined below.

1. For $nL_w(745) \le 0.1$ mW cm^{-2} μm^{-1} sr^{-1}, $Q(\lambda) = Q^{(QAA)}(\lambda)$
2. For $0.1 < nL_w(745) < 0.2$ mW cm^{-2} μm^{-1} sr^{-1}, $Q(\lambda) = Q^{(QAA)}(\lambda) + (10\ nL_w(745) - 1) \times (Q^{(NIR)}(\lambda) - Q^{(QAA)}(\lambda))$
3. For $nL_w(745) \ge 0.2$ mW cm^{-2} μm^{-1} sr^{-1}, $Q(\lambda) = Q^{(NIR)}(\lambda)$,

where $Q^{(QAA)}(\lambda)$ and $Q^{(NIR)}(\lambda)$ are the QAA- and NIR-based IOP algorithms, respectively. It is noted that $nL_w(\lambda)$ spectra can be easily converted to the remote-sensing reflectance $R_{rs}(\lambda)$, i.e., $R_{rs}(\lambda) = nL_w(\lambda)/F_0(\lambda)$, where $F_0(\lambda)$ is the extraterrestrial solar irradiance.

With the proposed method, optimal IOP retrievals for $b_{bp}(\lambda)$, $a_{ph}(\lambda)$, $a_{dg}(\lambda)$, and $a_t(\lambda)$ can be achieved. Note that IOP retrievals from satellite observations are prone to various uncertainties and noise. For example, it is possible that IOP retrievals from one IOP algorithm can fail when deriving negative values. In this case, retrievals from another IOP algorithm are used for deriving the corresponding IOP values.

The performance of the NIR-QAA combined IOP algorithm for $b_{bp}(\lambda)$ (Fig. 3a), $a_{ph}(\lambda)$ (Fig. 3b), $a_{dg}(\lambda)$ (Fig. 3c), and $a_t(\lambda)$ (Fig. 3d) with the comprehensive IOP data set is significantly improved. The NIR-QAA combined IOP algorithm can derive reasonably high-quality IOPs for all water types. In comparison to the QAA-based algorithm (Fig. 2), all four IOP parameters show

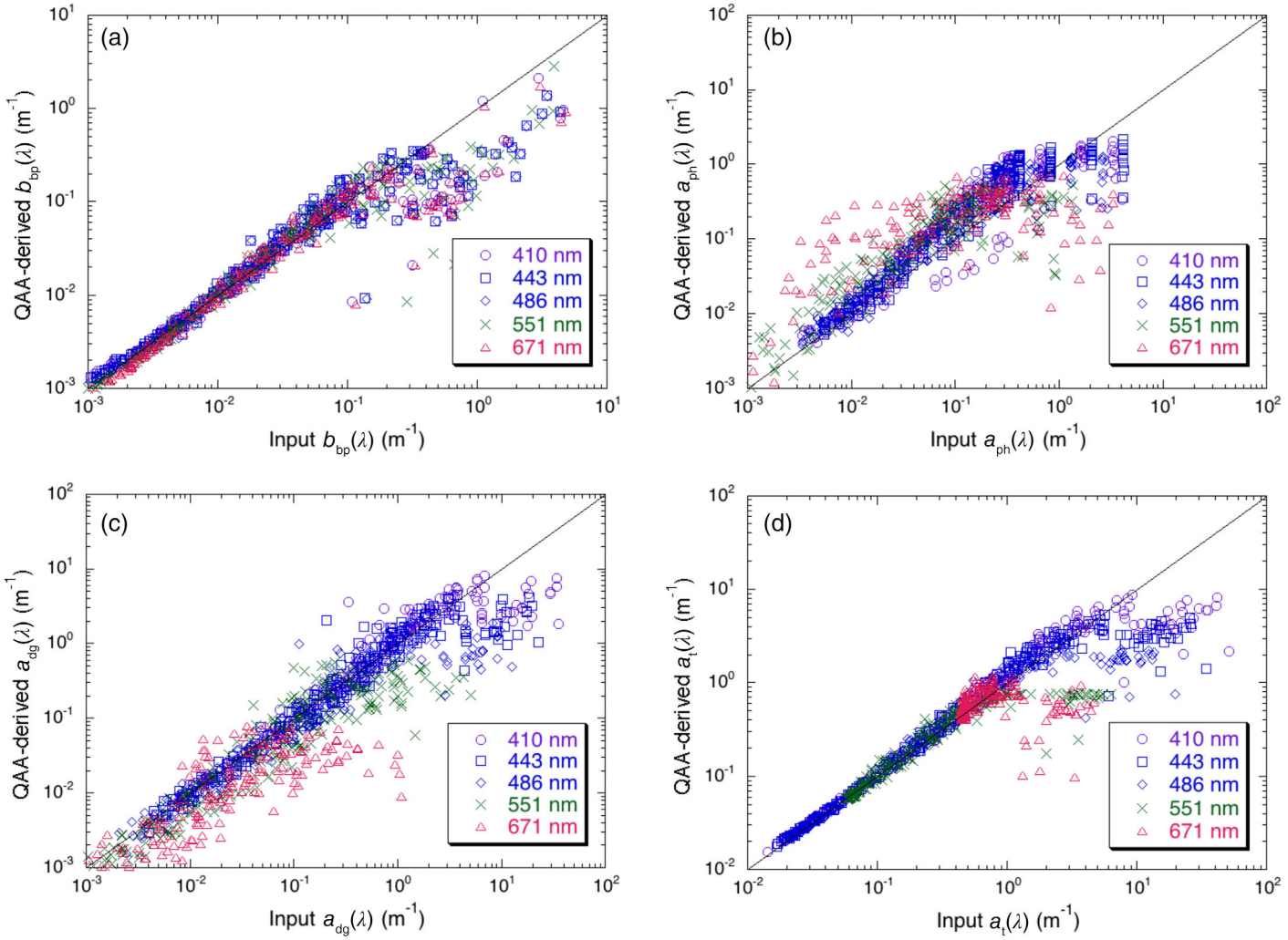

Fig. 2. Comparison of the QAA-based IOP retrievals with Hydrolight inputs (true values) at VIIRS spectral bands for (**a**) $b_{bp}(\lambda)$, (**b**) $a_{ph}(\lambda)$, (**c**) $a_{dg}(\lambda)$, and (**d**) $a_t(\lambda)$.

significant improvement in the turbid productive waters. On the other hand, the combined algorithm follows the QAA IOP algorithm and performs well in the clear open ocean. Since these two IOP algorithms can complement each other, the NIR-QAA combined IOP algorithm can take the advantages of the QAA algorithm in the open ocean and less turbid coastal waters and the advantages of the NIR-based algorithm in turbid coastal and inland waters.

Furthermore, the statistical evaluation shows that the good retrievals for all four IOP parameters can be achieved with the NIR-QAA combined IOP algorithm (Table 2). High-quality retrievals can be achieved for the IOP products of $b_{bp}(\lambda)$ and $a_t(\lambda)$ with the corresponding coefficients of determination R^2 at 0.952 and 0.936, respectively. Reasonably accurate $a_{ph}(\lambda)$ and $a_{dg}(\lambda)$ can be achieved with the NIR-QAA combined IOP algorithm. The R^2 values for the $a_{ph}(\lambda)$ and $a_{dg}(\lambda)$ are 0.723 and 0.738, respectively. This shows that retrievals of $a_{ph}(\lambda)$ and $a_{dg}(\lambda)$ with the NIR-QAA IOP algorithm are less accurate than those of $b_{bp}(\lambda)$ and $a_t(\lambda)$. Since the Hydrolight IOP data set covers a wide range of water types, the NIR-QAA combined IOP algorithm can be applied to the global satellite ocean color observations for deriving the IOP parameters for both open ocean and turbid coastal/inland waters.

Results

VIIRS-derived IOP products over the La Plata River Estuary

The La Plata River Estuary between Uruguay and Argentina is one of the most turbid regions in the world (Shi and Wang 2010). To further evaluate the performance of the IOP products from the QAA-based, NIR-based, and NIR-QAA combined IOP algorithms, the La Plata River Estuary region is selected to produce the IOP products from the three algorithms with VIIRS observations.

The different $b_{bp}(\lambda)$ products from the NIR-based IOP algorithm (Fig. 4a–e), the QAA-based IOP algorithm (Fig. 4f–h), and the NIR-QAA combined IOP algorithm (Fig. 4i–m) show that

Table 2. Statistics of the NIR-QAA combined IOP retrievals in comparison to Hydrolight inputs.

IOPs	Data number	Mean ratio	Median ratio	Ratio RMSD	Ratio MAPD	R^2
$b_{bp}(\lambda)$	664	1.001	0.972	0.123	0.078	0.952
$a_{ph}(\lambda)$	664	1.270	1.310	1.510	1.142	0.723
$a_{dg}(\lambda)$	664	1.012	0.855	0.486	0.033	0.738
$a_t(\lambda)$	664	1.045	1.007	0.126	0.086	0.936

MAPD, mean absolute percentage deviation; RMSD, root mean square deviation.

high-quality IOP products can be obtained with the NIR-QAA combined IOP algorithm. In general, QAA-derived $b_{bp}(\lambda)$ products are smooth and less noisy for the entire region. Note that there are no $b_{bp}(745)$ and $b_{bp}(862)$ data from the QAA-based algorithm. Figure 4a–e shows the NIR-based climatology $b_{bp}(\lambda)$ in this region. Indeed, $b_{bp}(\lambda)$ images with the NIR-based approach in the open ocean show high data noise especially for $b_{bp}(443)$ (Fig. 4a). Actually, $b_{bp}(443)$ (Fig. 4a), $b_{bp}(551)$ (Fig. 4b), and $b_{bp}(671)$ (Fig. 4c) are all derived from $b_{bp}(745)$ (Fig. 4d) and $b_{bp}(862)$ (Fig. 4e) with the NIR-based algorithm. Thus, small error and noise in $nL_w(745)$ and $nL_w(862)$ due to atmospheric correction can lead to significant uncertainties of $b_{bp}(\lambda)$ in visible bands in the offshore waters where $nL_w(745)$ and $nL_w(862)$ are close to 0. It is also noted that the NIR-based $b_{bp}(\lambda)$ in

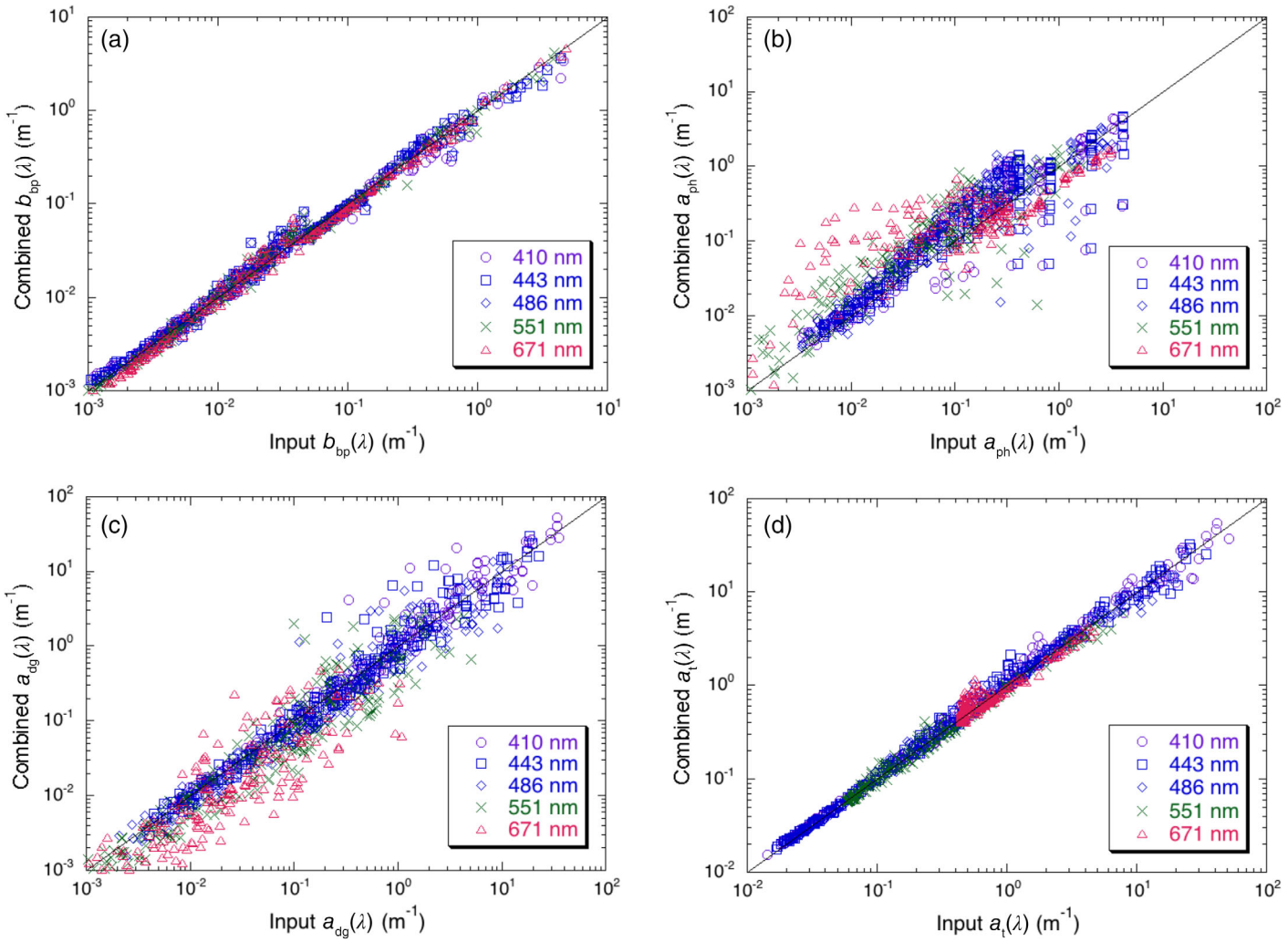

Fig. 3. Comparison of the NIR-QAA combined IOP retrievals with Hydrolight inputs (true values) at VIIRS spectral bands for (**a**) $b_{bp}(\lambda)$, (**b**) $a_{ph}(\lambda)$, (**c**) $a_{dg}(\lambda)$, and (**d**) $a_t(\lambda)$.

highly turbid waters (Fig. 4a–f) in the visible bands is ~ 4–5 times higher than those from the corresponding QAA-based $b_{bp}(\lambda)$ products (Fig. 4f–h).

The QAA- and NIR-based $b_{bp}(\lambda)$ results in Fig. 4 clearly demonstrate the advantages and disadvantages of each IOP algorithm. The QAA-based algorithm usually underestimates $b_{bp}(\lambda)$ and even loses its sensitivity to $b_{bp}(\lambda)$ change in moderately to highly turbid waters (Fig. 4f–h), while the NIR-based $b_{bp}(\lambda)$ retrievals show high data noise in the offshore waters in comparison with those from the QAA-based algorithm. This is consistent with the performance assessment using the comprehensive Hydrolight simulation data set as shown in Figs. 1, 2.

Figure 4i–m shows results of the NIR-QAA combined VIIRS climatology $b_{bp}(\lambda)$ at the bands 443 nm $b_{bp}(443)$ (Fig. 4i), 551 nm $b_{bp}(551)$ (Fig. 4j), and 671 nm $b_{bp}(671)$ (Fig. 4k), respectively. Note that the QAA IOP algorithm is specifically developed for IOP retrievals in the visible bands and not at the NIR bands. Since there are no QAA $b_{bp}(745)$ and $b_{bp}(862)$ data, $b_{bp}(745)$ (Fig. 4l) and $b_{bp}(862)$ (Fig. 4m) only show the areas with $nL_w(745) \geq 0.2$ mW cm^{-2} μm^{-1} sr^{-1} from the NIR-based IOP algorithm. In comparison with the NIR-based climatology $b_{bp}(\lambda)$, the NIR-QAA combined $b_{bp}(\lambda)$ products show significant improvement in the offshore region. In the estuarine regions, however, values of the NIR-QAA combined $b_{bp}(\lambda)$ become much higher than those from the QAA approach. Furthermore, no obvious data discontinuities can be found in the transition zones from the QAA $b_{bp}(\lambda)$ in the offshore open ocean to the NIR-based $b_{bp}(\lambda)$ in turbid coastal waters. This demonstrates that the proposed approach can provide the best $b_{bp}(\lambda)$ data quality for both open ocean and turbid coastal/inland waters.

Phytoplankton absorption coefficient $a_{ph}(\lambda)$ is another IOP product derived from the VIIRS observations. Figure 5 shows the VIIRS climatology $a_{ph}(443)$, $a_{ph}(551)$, and $a_{ph}(671)$ data derived from the NIR-based IOP algorithm (Fig. 5a–c), QAA-based IOP algorithm (Fig. 5d–f), and NIR-QAA combined IOP algorithm (Fig. 5g–i). Again, high noise in the NIR-based $a_{ph}(443)$ is obvious in the offshore waters (Fig. 5a). In the La Plata River Estuary, the QAA-based $a_{ph}(443)$ (Fig. 5d) is similar to those of the NIR-based $a_{ph}(443)$ (Fig. 5a). However, the QAA-based $a_{ph}(551)$ (Fig. 5e) and $a_{ph}(671)$ (Fig. 5f) are visibly lower than the corresponding NIR-based $a_{ph}(551)$ (Fig. 5b) and $a_{ph}(671)$ (Fig. 5c) in turbid waters. This is also consistent with the results from Hydrolight simulations in Figs. 1, 2. The NIR-QAA combined $a_{ph}(443)$ (Fig. 5g), $a_{ph}(551)$ (Fig. 5h), and $a_{ph}(671)$ (Fig. 5i) show improvements in $a_{ph}(\lambda)$ for both the offshore open ocean and estuarine turbid water region.

Figure 6 shows the VIIRS climatology $a_{dg}(443)$, $a_{dg}(551)$, and $a_{dg}(671)$ products derived from the NIR-based IOP algorithm

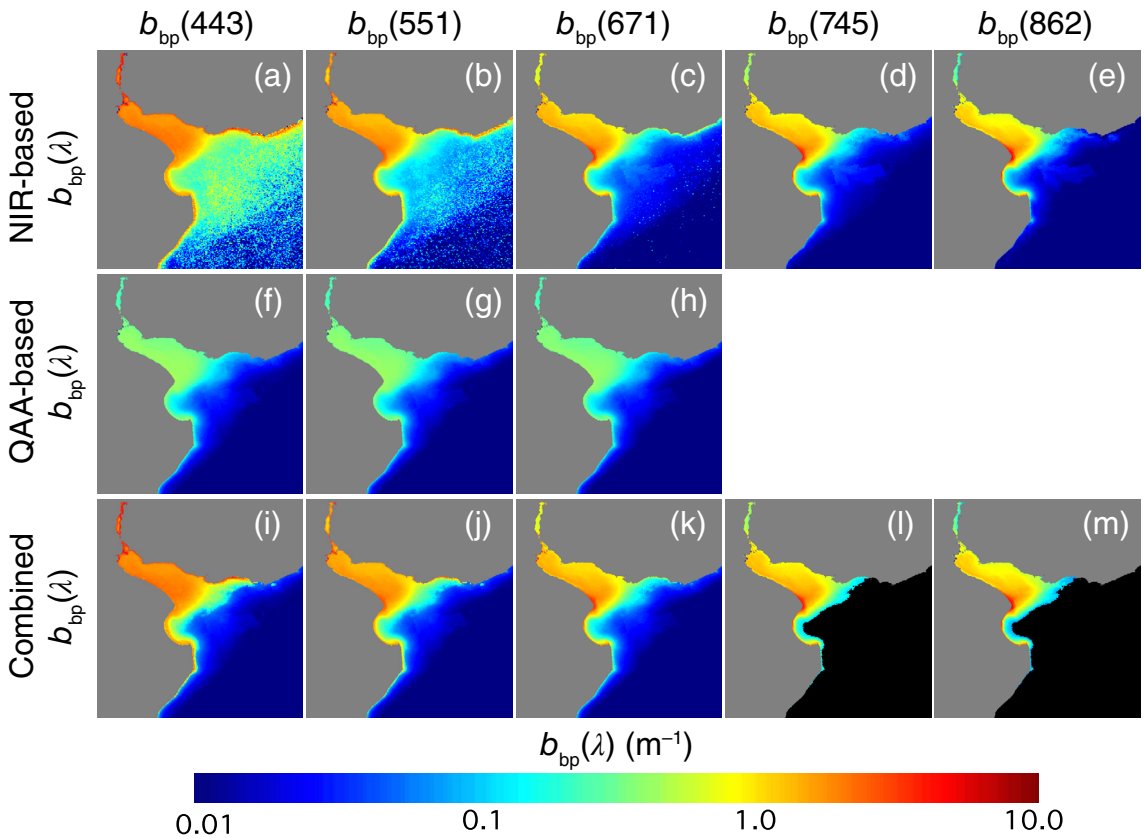

Fig. 4. VIIRS-measured climatology $b_{bp}(\lambda)$ at various VIIRS bands in the La Plata River Estuary derived using the approaches of (**a**–**e**) the NIR-based IOP algorithm, (**f**–**h**) the QAA-based IOP algorithm, and (**i**–**m**) the NIR-QAA combined IOP algorithm.

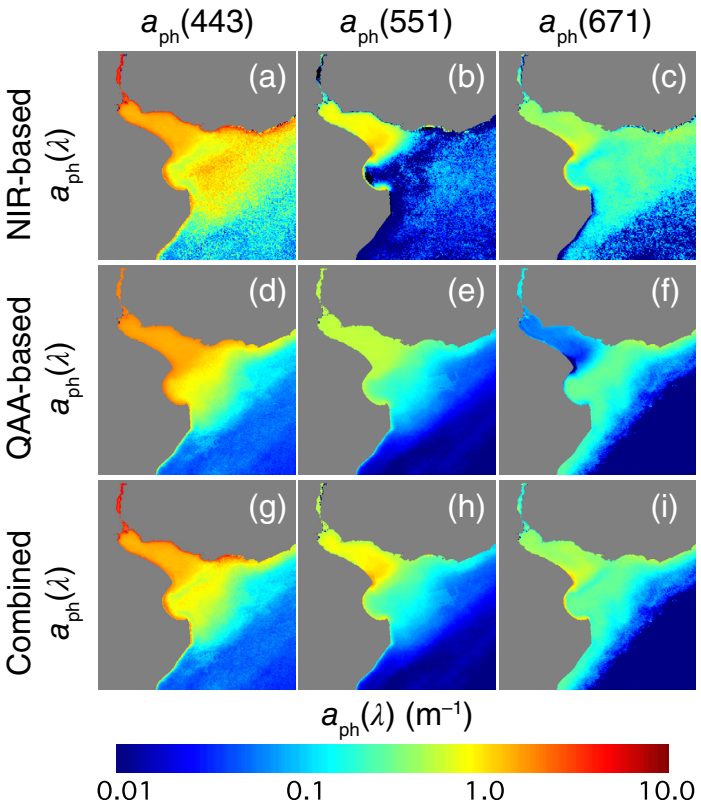

Fig. 5. VIIRS-measured climatology $a_{ph}(\lambda)$ at various VIIRS bands in the La Plata River Estuary derived using the approaches of (**a–c**) the NIR-based IOP algorithm, (**d–f**) the QAA-based IOP algorithm, and (**g–i**) the NIR-QAA combined IOP algorithm.

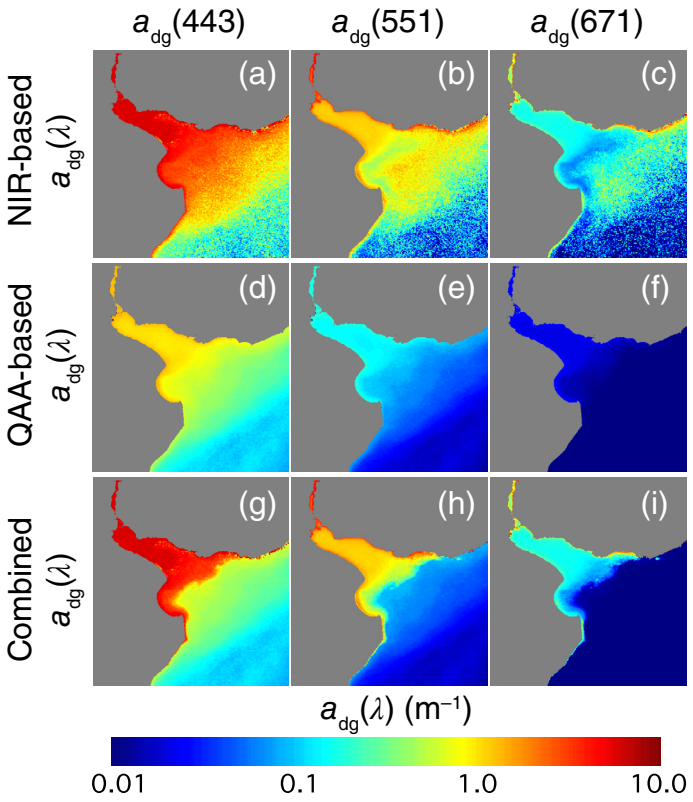

Fig. 6. VIIRS-measured climatology $a_{dg}(\lambda)$ at various VIIRS bands in the La Plata River Estuary derived using the approaches of (**a–c**) the NIR-based IOP algorithm, (**d–f**) the QAA-based IOP algorithm, and (**g–i**) the NIR-QAA combined IOP algorithm.

(Fig. 6a–c), QAA-based IOP algorithm (Fig. 6d–f), and NIR-QAA combined IOP algorithm (Fig. 6g–i). Similar to Figs. 4a–c, 5a–c, the QAA-derived $a_{dg}(\lambda)$ (Fig. 6d–f) has much less noise than those from the NIR-based algorithm (Fig. 6a–c) in the open ocean. However, the QAA-based $a_{dg}(\lambda)$ values in the La Plata River Estuary are much less than those of the NIR-based $a_{dg}(\lambda)$. The QAA-based and NIR-based $a_{dg}(\lambda)$ in the La Plata River Estuary are consistent with the Hydrolight simulations in Figs. 1, 2, which show that the QAA-based $a_{dg}(\lambda)$ significantly underestimates $a_{dg}(\lambda)$, while the NIR-based $a_{dg}(\lambda)$ is close to the sea truth in turbid waters.

On the other hand, high noise in the NIR-based $a_{dg}(\lambda)$ shown in Fig. 6a–c for the offshore waters is the retrieval artifact due to the insignificant $nL_w(\lambda)$ at the VIIRS NIR bands as suggested by the Hydrolight simulations (Fig. 1). In contrast, the QAA-based $a_{dg}(\lambda)$ in the offshore waters is reliable and accurate. The NIR-QAA combined $a_{dg}(\lambda)$ images in this region (Fig. 6g–i) show the high quality of $a_{dg}(\lambda)$ for both the turbid estuarine waters and the offshore waters. In fact, there are no $a_{dg}(\lambda)$ data gaps from the NIR-QAA combined algorithm.

Figure 7 shows the VIIRS-SNPP climatology $a_t(443)$, $a_t(551)$, and $a_t(671)$ products derived from the NIR-based IOP algorithm (Fig. 7a–c), QAA-based IOP algorithm (Fig. 7d–f), and NIR-QAA combined IOP algorithm (Fig. 7g–i), respectively. Note that $a_t(\lambda) = a_{ph}(\lambda) + a_{dg}(\lambda) + a_w(\lambda)$, and $a_w(\lambda)$ can play a significant role in the total absorption coefficient $a_t(\lambda)$ at the VIIRS 551 and 671 nm bands especially for the open ocean. The NIR-based $a_t(\lambda)$ indeed shows high noise $a_t(\lambda)$ retrievals in the offshore clear waters in Fig. 7a–c. The Hydrolight simulations for the NIR-based $a_t(\lambda)$ retrievals in Fig. 1d also suggest that $a_t(\lambda)$ derived from the NIR-based IOP algorithm in the offshore open ocean can be erroneous. In comparison, the QAA-based $a_t(\lambda)$ in the open ocean is good data quality in terms of both the noise level and data accuracy (Fig. 2d).

The QAA-based $a_t(\lambda)$ shows low noise for the coastal and estuarine turbid regions as well as for the open ocean. However, the QAA-based $a_t(\lambda)$ (Fig. 7d–f) in the La Plata River Estuary is significantly lower than the corresponding NIR-based $a_t(\lambda)$ (Fig. 7a–c). As an example, the QAA-based $a_t(551)$ (Fig. 7e) in the estuary is generally ~ 0.5 m^{-1} or less, while the NIR-based $a_t(551)$ (Fig. 7b) in the estuary is ~ 2.5 m^{-1}. This is also consistent with the Hydrolight simulations for turbid waters shown in Figs. 1d, 2d.

Figure 7g–i shows IOP results from the NIR-QAA combined $a_t(\lambda)$ in the La Plata River Estuary. With the combination of the QAA-based $a_t(\lambda)$ for offshore oceans and NIR-based $a_t(\lambda)$ for coastal and estuarine waters, good quality $a_t(\lambda)$ data for the entire

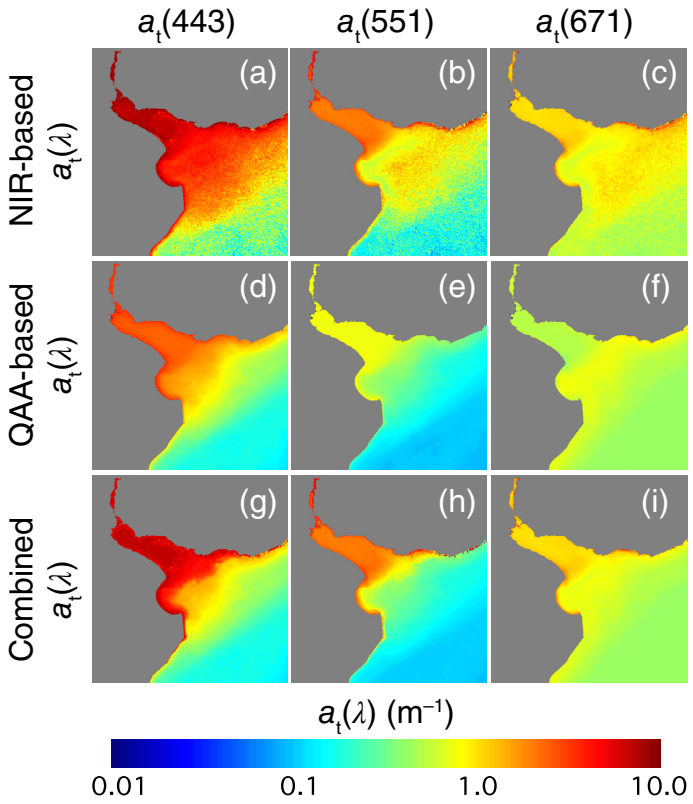

Fig. 7. VIIRS-measured climatology $a_t(\lambda)$ at various VIIRS bands in the La Plata River Estuary derived using the approaches of (**a**–**c**) the NIR-based IOP algorithm, (**d**–**f**) the QAA-based IOP algorithm, and (**g**–**i**) the NIR-QAA combined IOP algorithm.

region are obtained. Specifically, combined $a_t(\lambda)$ keeps high-quality $a_t(\lambda)$ from the NIR-based IOP algorithm in the La Plata River Estuary and high-quality $a_t(\lambda)$ from the QAA-based IOP algorithm in the offshore region. In the La Plata River Estuary, $a_t(443)$, $a_t(551)$, and $a_t(671)$ can reach ~ 5 m^{-1}, 2.5 m^{-1}, and 1.5 m^{-1}, respectively. Indeed, with the NIR-QAA combined IOP algorithm, the less noisy and more accurate $a_t(\lambda)$ in offshore open ocean waters from the QAA IOP algorithm is chosen to produce high-quality $a_t(\lambda)$ for the entire region.

A few studies have been conducted in the La Plata River Estuary region. The TSM concentration and the turbidity from the satellite ocean color observations and the in situ measurements (Moreira et al. 2013; Dogliotti et al. 2016) indeed show significant enhancements in the inner and middle La Plata River Estuary due to the river discharge and wind-driven sediment resuspension. The spatial pattern of the TSM concentration and turbidity in these studies are consistent with the $b_{bp}(\lambda)$ pattern in Fig. 4i–m and $a_{dg}(\lambda)$ pattern in Fig. 6g–i. Since both $b_{bp}(\lambda)$ and $a_{dg}(\lambda)$ are proportional to the particle concentrations in the water column, the consistence between the IOP products in this study and the measurements of TSM and turbidity qualitatively suggests that the IOP products in the La Plata River Estuary from the NIR-QAA combined method as shown in Figs. 4–7 are reasonably accurate.

The NIR-QAA combined IOP products in the other coastal regions

VIIRS-SNPP IOP products $b_{bp}(\lambda)$, $a_{ph}(\lambda)$, $a_{dg}(\lambda)$, and $a_t(\lambda)$ derived from the QAA-based algorithm, NIR-based algorithm, and NIR-QAA combined algorithm in the La Plata Estuary region have different performances as shown in Figs. 4–7. Results show that the NIR-QAA blended IOP algorithm can produce high-quality $b_{bp}(\lambda)$, $a_{ph}(\lambda)$, $a_{dg}(\lambda)$, and $a_t(\lambda)$ for both offshore open ocean waters and turbid coastal waters. To further evaluate the applicability of the NIR-QAA combined IOP algorithm for the global ocean, China's east coastal region, the US east coastal region, and the Mississippi River Estuary region are selected to evaluate IOPs of $b_{bp}(\lambda)$, $a_t(\lambda)$, $a_{dg}(\lambda)$, and $a_{ph}(\lambda)$ using the NIR-QAA combined IOP algorithm.

The climatology $b_{bp}(\lambda)$, $a_{ph}(\lambda)$, $a_{dg}(\lambda)$, and $a_t(\lambda)$ from the combined IOP algorithm in China's east coastal region at the VIIRS-SNPP bands of 443, 551, and 671 nm are also derived (Fig. 8). China's east coastal regions feature a high loading of sediment concentration (Shi and Wang 2010, 2012) such as in the regions of the Hangzhou Bay, Yangtze River Estuary, and Subei Shoal in the continental shelf (Milliman and Meade 1983; Milliman et al. 1985). In fact, TSM concentrations can reach over 1000 g m^{-3} in some regions (Shen et al. 2010*b*; Zhang et al. 2010*a*). Farther offshore, the ocean is featured with clear open ocean waters with Kuroshio Current flowing from the southwest direction to the northeast direction. The CDOM absorption coefficient at the wavelength of 400 nm $a_{CDOM}(400)$ ranges approximately from greater than 1 m^{-1} in the coastal region to near 0 m^{-1} in the open ocean (Gong 2004).

For all the products of $b_{bp}(\lambda)$, $a_t(\lambda)$, $a_{dg}(\lambda)$, and $a_{ph}(\lambda)$, the noise level is low for both coastal and offshore waters. $b_{bp}(\lambda)$ reaches over ~ 2 m^{-1} in highly turbid waters. In the Hangzhou Bay, Subei Shoal, and Yangtze River Estuary enhanced $a_{dg}(443)$ (Fig. 8c) and $a_t(443)$ (Fig. 8d) can be over ~ 4 m^{-1}, while $a_{ph}(443)$ (Fig. 8b) only shows moderate increase in comparison to $a_{ph}(443)$ in the open ocean. This further suggests that high $a_t(\lambda)$ in coastal waters is attributed to the enhanced absorption of the dissolved and detrital matter, which are driven by the river runoff and sediment resuspensions in the Hangzhou Bay, Yangtze River Estuary, and Subei Shoal. Phytoplankton bloom is not a major cause for the features of enhanced $a_t(\lambda)$ along China's east coastal region. It is also noted that $a_t(671)$ in the open ocean is significantly higher than the $a_t(443)$ and $a_t(551)$ because $a_w(671)$ is much larger than $a_w(443)$ and $a_w(551)$. In the turbid China's east coastal region, $b_{bp}(\lambda)$ values generally become flat spectrally or slightly increase from $b_{bp}(443)$ (Fig. 8a) to $b_{bp}(671)$ (Fig. 8i). This implies that the power law exponential slope η of $b_{bp}(\lambda)$ is slightly negative or close to 0 (Shi and Wang 2014, 2017, 2019), and further suggests that the particle size in the water column of the highly turbid waters is generally larger than that of the other coastal regions.

Similarly, Fig. 9 shows the climatology $b_{bp}(\lambda)$, $a_{ph}(\lambda)$, $a_{dg}(\lambda)$, and $a_t(\lambda)$ in the Mississippi River Estuary and tributaries from VIIRS-SNPP observations using the NIR-QAA combined IOP algorithm. Even though the IOP features in this region are not as

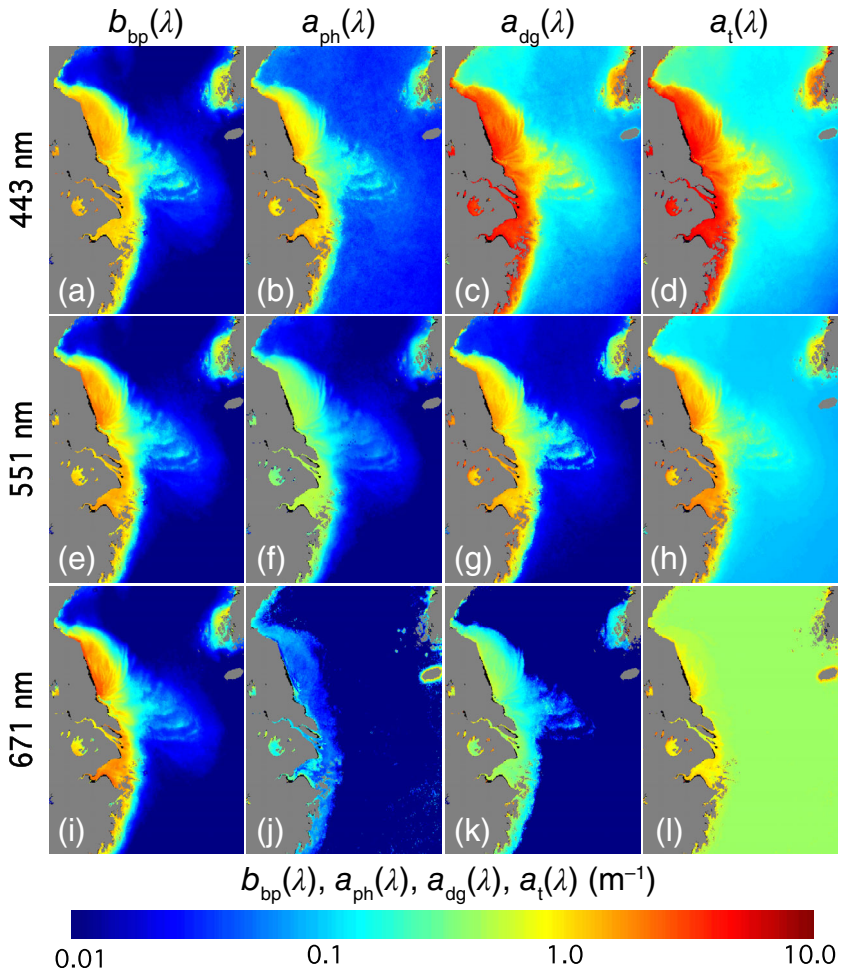

Fig. 8. VIIRS-measured climatology $b_{bp}(\lambda)$, $a_{ph}(\lambda)$, $a_{dg}(\lambda)$, and $a_t(\lambda)$ in China's east coastal region derived using the NIR-QAA combined IOP algorithm for VIIRS bands at (**a**–**d**) 443 nm, (**e**–**h**) 551 nm, and (**i**–**l**) 671 nm.

pronounced as in China's east coastal region, enhanced $a_{dg}(443)$ (Fig. 9c) and $a_t(443)$ (Fig. 9d) can still be observed in the Mississippi River Estuary, Lake Pontchartrain, and Atchafalaya River Estuary. Similar to China's east coastal region, $a_{dg}(\lambda)$ (Fig. 9c,g,k) is the dominant component of $a_t(\lambda)$ (Fig. 9d,h,l). However, $a_{ph}(443)$ in this region (Fig. 9b) is generally higher than $a_{ph}(443)$ in China's east coastal region (Fig. 8b). Thus, its contribution to $a_t(443)$ in this region is not negligible. Higher $a_{ph}(\lambda)$ in this region also suggests that coastal and inland waters around the Mississippi River Estuary and its tributaries are more productive than China's east coastal region and La Plata River Estuary, even though the waters are less turbid than those two regions in terms of $b_{bp}(\lambda)$ and $nL_w(\lambda)$ magnitudes (Shi and Wang 2010, 2017). Different from the $b_{bp}(\lambda)$ spectra in turbid waters along China's east coastal region, $b_{bp}(\lambda)$ values generally decrease with the increase of wavelength, e.g., from $b_{bp}(443)$ (Fig. 9a) to $b_{bp}(671)$ (Fig. 9i). This shows that the power law exponential slope η for $b_{bp}(\lambda)$ is positive in the Mississippi River Estuary, Lake Pontchartrain, and Atchafalaya River Estuary, while it is negative in China's east coastal region (Shi and Wang 2019). Since power law exponential slope η of $b_{bp}(\lambda)$ is related to the particle size distribution slope ξ in the water column (Kostadinov et al. 2009), the polynomial relationship between η and ξ implies that the particle size in the Mississippi River Estuary and tributaries is smaller than that in China's east coastal region (Shi and Wang 2019).

Finally, climatology $b_{bp}(\lambda)$, $a_{ph}(\lambda)$, $a_{dg}(\lambda)$, and $a_t(\lambda)$ derived from the NIR-QAA combined IOP algorithm in the US east coastal region are shown in Fig. 10. Similar to the other regions discussed previously, these IOP products are in good quality with little noise for both the open ocean and turbid coastal waters. In comparison to the La Plata River Estuary region (Figs. 4–7), China's east coastal region (Fig. 8), and Mississippi River Estuary and tributaries (Fig. 9), the US east coastal region is less turbid with moderately high $b_{bp}(\lambda)$ in the Chesapeake Bay, Delaware Bay, and Pamlico Sound. Highly turbid waters at the tips of the Chesapeake Bay, Delaware Bay, and Albemarle Sound with $b_{bp}(443)$ over ~ 2 m^{-1} can also be observed.

In the Chesapeake Bay and Delaware Bay, $a_{dg}(443)$ and $a_{ph}(443)$ are in the same order. This is different from the other highly turbid regions such as the La Plata River Estuary, China's

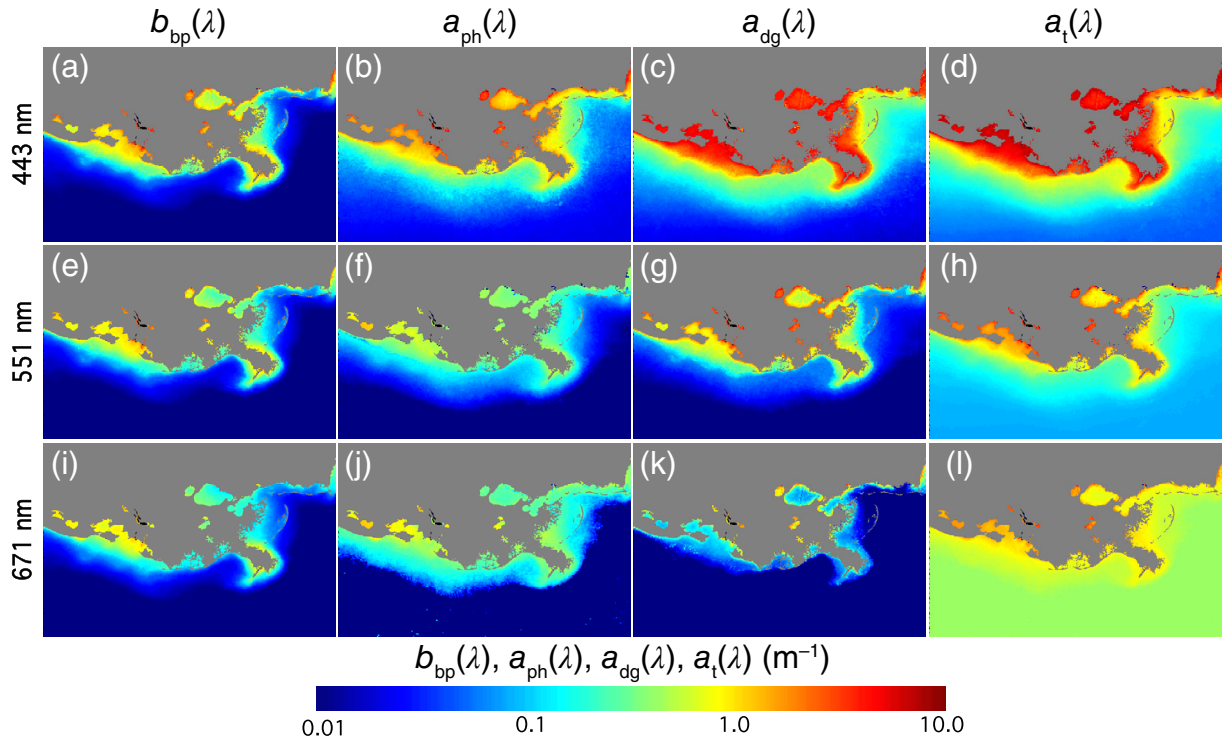

Fig. 9. VIIRS-measured climatology $b_{bp}(\lambda)$, $a_{ph}(\lambda)$, $a_{dg}(\lambda)$, and $a_t(\lambda)$ in the Mississippi River Estuary and tributaries derived using the NIR-QAA combined IOP algorithm for VIIRS bands at (**a**–**d**) 443 nm, (**e**–**h**) 551 nm, and (**i**–**l**) 671 nm.

east coast region, and Mississippi River Estuary where $a_{dg}(443)$ is the dominant component in $a_t(443)$. In the US east coastal region, $a_{dg}(443)$ (Fig. 10c) is also significantly higher than $a_{ph}(443)$ (Fig. 10b) in the Pamlico Sound. This indicates that river runoff and sediment resuspension is the major process that drives $a_{dg}(443)$ in the Pamlico Sound, while high productivity and phytoplankton bloom in the Chesapeake Bay and Delaware Bay can lead to elevated $a_{ph}(443)$. Climatology $a_t(\lambda)$ images (Fig. 10d,h,l) show that $a_t(443)$ reaches over ~ 3 m^{-1} in these turbid areas. Broadly enhanced $a_t(\lambda)$ can also be found in most parts of the Chesapeake Bay, Delaware Bay, and Pamlico Sound regions.

The IOP products in China's east coastal region, the Mississippi River Estuary, and the Chesapeake Bay as shown in Figs. 8–10 are consistent with the observations from various studies in these three regions (D'Sa et al. 2007; Werdell et al. 2009; Zhang et al. 2010*b*, 2012). In China's east coastal region, the IOP values in Fig. 8 qualitatively agree with the in situ measurements in the region (Zhang et al. 2010*b*) and also specifically in Lake Taihu (Zhang et al. 2012). In the Mississippi River Estuary, $b_{bp}(\lambda)$ slope from the blue to red bands as indicated in Fig. 9 is similar to the observations (D'Sa et al. 2007), and high $a_{dg}(\lambda)$ and $b_{bp}(\lambda)$ values are found in the Atchafalaya River Estuary since the sediment plume is trapped within the coastal current (Falcini et al. 2012). In the Chesapeake Bay, $a_{ph}(\lambda)$ trends lower from the upper Chesapeake Bay to the lower Chesapeake Bay as shown in Fig. 10. This agrees with the observations of the spatial variation of Chl *a* in the region (Werdell et al. 2009). On the other hand, Tzortziou et al. (2006) show that measured and model-estimated water-leaving radiances agree with each other very well in the Chesapeake Bay. This further suggests that the IOP retrievals from the bio-optical models as shown in this study are expected to match well with the sea truth.

Discussion

$nL_w(\lambda)$ spectra are determined by the constituents of seawaters such as CDOM, phytoplankton particles, inorganic mineral sediments, and so on. The specific spectral features of each constituent such as absorption coefficients, e.g., $a_{ph}(\lambda)$, $a_{dg}(\lambda)$, and $a_t(\lambda)$, and backscattering coefficients, e.g., $b_{bp}(\lambda)$, determine the spectral variability of $nL_w(\lambda)$ or remote-sensing reflectance just beneath the surface $r_{rs}(\lambda)$.

Coastal waters with a diffuse attenuation coefficient $K_d(490) > 1$ m^{-1} in the global ocean can account for about 1/7 of the global continental shelf (Shi and Wang 2010). Considering that coastal waters are often featured with complexity of the seawater constituents as well as the dynamic variability, it is critical to derive accurate IOP parameters in coastal waters in order to study climatic, hydrological, physical, biological, and biogeochemical processes and their interactions with each other. From this point of view, the new NIR-QAA IOP algorithm can broadly improve the global satellite IOP products in the global continental shelf region instead of just some highly turbid estuarine regions.

To derive all IOP parameters in the entire spectrum from the blue to the NIR bands in coastal and inland waters, it is a

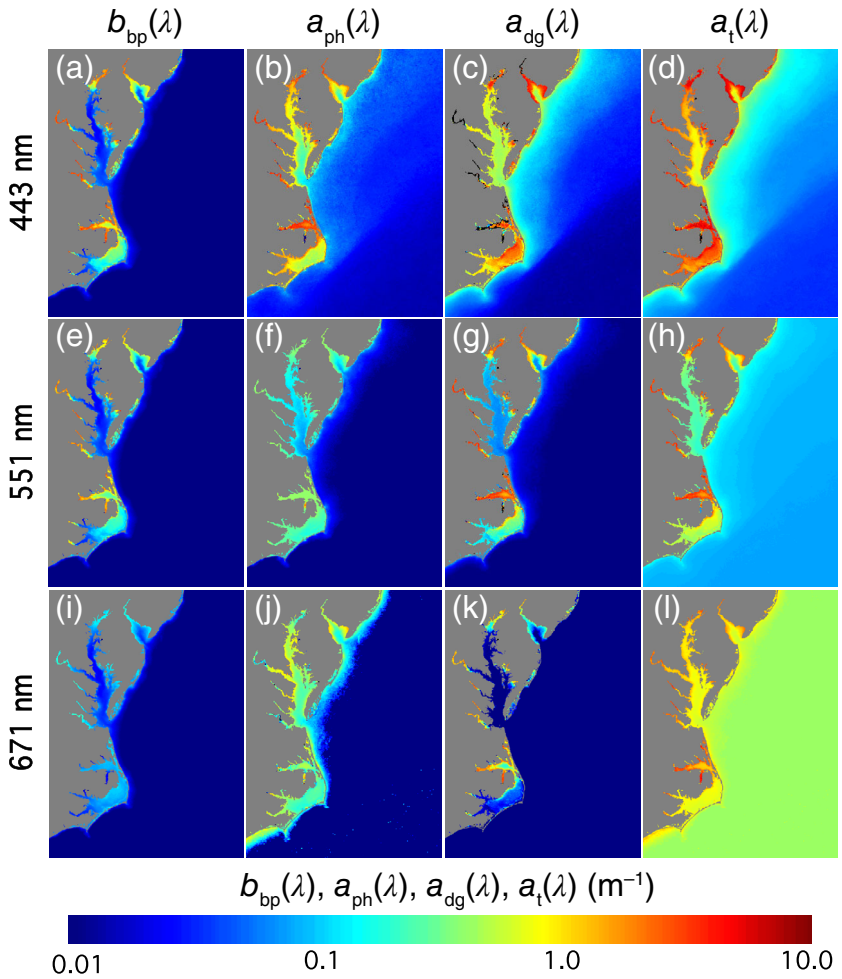

Fig. 10. VIIRS-measured climatology $b_{bp}(\lambda)$, $a_{ph}(\lambda)$, $a_{dg}(\lambda)$, and $a_t(\lambda)$ in US east coastal region derived using the NIR-QAA combined IOP algorithm for VIIRS bands at (**a**–**d**) 443 nm, (**e**–**h**) 551 nm, and (**i**–**l**) 671 nm.

prerequisite to compute $b_{bp}(\lambda)$ first. Even though the power law of $b_{bp}(\lambda)$ has been widely used in the IOP modeling effort, it has been typically a challenge to accurately estimate reference $b_{bp}(\lambda_0)$ and $b_{bp}(\lambda)$ power law exponential slope η directly with the ocean reflectance in the visible bands. As shown previously, $b_{bp}(\lambda_0)$ and η in the QAA algorithm are computed using ocean reflectance in the visible bands empirically (Lee et al. 2002; IOCCG 2006), while η is set to a constant value in the GSM IOP algorithm (Garver and Siegel 1997; Maritorena et al. 2002). Sensitivity studies have shown that η can significantly affect the accuracy of IOP retrievals (Hoge and Lyon 1996). In addition, satellite-derived $nL_w(\lambda)$ spectra in the visible bands become less-related or even totally unrelated to the seawater constituent changes when $nL_w(\lambda)$ at the NIR wavelength is over a certain value (Shi and Wang 2009*a*, 2014; Shen et al. 2010*a*). This suggests that IOP algorithms such as QAA and GSM using $nL_w(\lambda)$ at the visible bands have some significant limitations in deriving accurate water IOPs in turbid coastal and inland waters.

In comparison, the NIR-based IOP algorithm for turbid coastal and inland waters in this study is essentially analytical since the spectral features of the seawater constituents in the NIR wavelengths are used in this algorithm. Since it can compute the η values directly, this algorithm can effectively address the large variation of η values (Reynolds et al. 2001; Wozniak and Stramski 2004; Shi and Wang 2017). Otherwise, the η variation can lead to notable errors with empirical or semi-analytical IOP approaches.

A recent study (Shi and Wang 2017) has shown that the NIR-based $b_{bp}(\lambda)$ algorithm can be applied to highly turbid waters to derive reasonably accurate $b_{bp}(\lambda)$ in the visible and NIR bands. It can be safely used for highly turbid waters with $nL_w(745)$ and $nL_w(862)$ less than ~ 6 mW cm^{-2} μm^{-1} sr^{-1} and ~ 4 mW cm^{-2} μm^{-1} sr^{-1}, respectively. The Hydrolight simulations show that the NIR-based algorithm not only can be used to derive $b_{bp}(\lambda)$ spectra, but also other IOP parameters such as $a_{ph}(\lambda)$ and $a_{dg}(\lambda)$ with reasonably good accuracy over highly turbid waters. On the other hand, atmospheric correction uncertainty in the VIIRS NIR bands can be significant for $nL_w(745)$ and $nL_w(862)$ in clear open ocean where their values are close to 0. This determines that the NIR-based IOP algorithm is not applicable in the open ocean.

To evaluate the performance of the VIIRS NIR-QAA combined IOP retrievals, the in situ IOP data coincident with the VIIRS measurements are required. However, some available data sets such as Nechad et al. (2015) and Valente et al. (2016) do not have the corresponding IOP measurements in the VIIRS era from 2012. In addition, these data sets lack the corresponding $nL_w(\lambda)$ data in the NIR wavelengths. Due to the unavailability of the in situ $b_{bp}(\lambda)$ data in the turbid waters, and also the low diversity and high uncertainty of the in situ $b_{bp}(\lambda)$, $a_{ph}(\lambda)$, and $a_{dg}(\lambda)$ measurements, we used the expanded IOCCG data set to evaluate the performance of the NIR-based, QAA-based, and NIR-QAA combined IOP algorithms. The expanded IOCCG data set covers a variety of water types from the open ocean to coastal productive and turbid waters. The diversity of water types in the Hydrolight simulations is necessary in order to evaluate the performance of these IOP algorithms for global ocean applications. It avoids the limitation of using the in situ data which may be more suitable for developing a regional IOP algorithm, but is not diversified enough to cover various water types in order to develop a generic IOP algorithm applicable for the global ocean. The good performance of the NIR-QAA combined algorithm in the Hydrolight data set provides the evidence that the new combined IOP algorithm can be applied to satellite ocean color observations for deriving IOP parameters for the global ocean.

In addition, the uncertainty and biases might exist for IOP retrievals from the NIR-QAA algorithm from the global VIIRS observations. This can largely come from the complexity of the coastal waters in terms of the IOP spectral features even though $b_{bp}(\lambda)$ power law exponential slope η can be well quantified and characterized with the $b_{bp}(\lambda)$ at the NIR 745 and 862 nm. In this study, dynamic spectral shapes of $a_{ph}(\lambda)$ and $a_{dg}(\lambda)$ are characterized with the empirical formulas for $a_{ph}(410)/a_{ph}(443)$ and $a_{dg}(410)/a_{dg}(443)$ following the same approach in the QAA IOP algorithm. These two empirical formulas are derived from the IOCCG IOP test data set (IOCCG 2006), which is dominated with the clear open ocean and less turbid coastal waters. Thus, cautions of possible uncertainties and biases should be given when the NIR-QAA combined IOP algorithm is applied to various coastal waters especially highly turbid waters. In situ IOP measurements might be necessary in order to further tune the coefficients and develop a regional IOP algorithm to produce regional-specific high-quality IOP products from satellite ocean color observations.

Summary

In this study, we developed a NIR-QAA combined IOP algorithm for global ocean applications. The NIR-based IOP algorithm is based on the fact that the water absorption coefficients $a_w(\lambda)$ at the NIR wavelengths are generally much larger than other absorption components. The NIR-based IOP algorithm is assessed and compared with the QAA-based IOP algorithm using the Hydrolight simulated data, showing that the NIR-based algorithm produces significantly improved IOP data over turbid coastal and inland waters.

The advantages of the NIR-based and QAA-based algorithms are also addressed and evaluated. A combination of the NIR-based and QAA-based algorithms has been proposed and demonstrated. We used the La Plata River Estuary as an example to show the performance for IOPs of $b_{bp}(\lambda)$, $a_{ph}(\lambda)$, $a_{dg}(\lambda)$, and $a_t(\lambda)$ retrievals with the NIR-based, QAA-based, and NIR-QAA combined IOP algorithms. The NIR-QAA combined algorithm for $b_{bp}(\lambda)$, $a_{ph}(\lambda)$, $a_{dg}(\lambda)$, and $a_t(\lambda)$ in the La Plata River Estuary region shows that high-quality IOP products of $b_{bp}(\lambda)$ $a_{ph}(\lambda)$, $a_{dg}(\lambda)$, and $a_t(\lambda)$ can be produced for both the open ocean and turbid coastal/inland waters.

Using the NIR-QAA combined IOP algorithm, we also produce the IOP products of $b_{bp}(\lambda)$, $a_{ph}(\lambda)$, $a_{dg}(\lambda)$, and $a_t(\lambda)$ in China's east coastal region, the US east coastal region, and the region of Mississippi River Estuary and tributaries with VIIRS-SNPP observations between 2012 and 2017. VIIRS-SNPP IOP results demonstrate that the NIR-QAA combined IOP algorithm can be used to routinely generate high-quality operational IOP products for the global ocean from satellite ocean color observations.

References

Bowers, D. G., and C. E. Binding. 2006. The optical properties of mineral suspended particles: A review and synthesis. Estuar. Coast. Shelf Sci. **67**: 219–230. doi:10.1016/j.ecss.2005.11.010.

Clark, D. K., H. R. Gordon, K. J. Voss, Y. Ge, W. Broenkow, and C. Trees. 1997. Validation of atmospheric correction over the oceans. J. Geophys. Res. Atmos. **102**: 17209–17217. doi:10.1029/96JD03345.

Dogliotti, A., K. G. Ruddick, B. Nechad, D. Doxaran, and E. Knaeps. 2015. A single algorithm to retrieve turbidity from remotely-sensed data in all coastal and estuarine waters. Remote Sens. Environ. **156**: 157–168. doi:10.1016/j.rse.2014.09.020.

Dogliotti, A. I., K. Ruddick, and R. Guerrero. 2016. Seasonal and inter-annual turbidity variability in the Rio de la Plata from 15 years of MODIS: El Nino dilution effect. Estuar. Coast. Shelf Sci. **182**: 27–39. doi:10.1016/j.ecss.2016.09.013.

Doron, M., S. Belanger, D. Doxaran, and M. Babin. 2011. Spectral variations in the near-infrared ocean reflectance. Remote Sens. Environ. **115**: 1617–1631. doi:10.1016/j.rse.2011.01.015.

D'Sa, E. J., R. L. Miller, and B. A. Mckee. 2007. Suspended particulate matter dynamics in coastal waters from ocean color: Application to the northern Gulf of Mexico. Geophys. Res. Lett. **34**. doi:10.1029/2007GL031192.

Eisma, D., and others. 1990. A camera and image-analysis system for in situ observation of flocs in natural waters. Neth. J. Sea Res. **27**: 43–56. doi:10.1016/0077-7579(90)90033-D.

Falcini, F., and others. 2012. Linking the historic 2011 Mississippi River flood to coastal wetland sedimentation. Nat. Geosci. **5**: 803–807. doi:10.1038/Ngeo1615.

Garver, S. A., and D. A. Siegel. 1997. Inherent optical property inversion of ocean color spectra and its biogeochemical interpretation. 1. Time series from the Sargasso Sea. J. Geophys. Res. Oceans **102**: 18607–18625. doi:10.1029/96JC03243.

Gitelson, A. A., J. F. Schalles, and C. M. Hladik. 2007. Remote chlorophyll-a retrieval in turbid, productive estuaries: Chesapeake Bay case study. Remote Sens. Environ. **109**: 464–472. doi:10.1016/j.rse.2007.01.016.

Goldberg, M. D., H. Kilcoyne, H. Cikanek, and A. Mehta. 2013. Joint Polar Satellite System: The United States next generation civilian polar-orbiting environmental satellite system. J. Geophys. Res. Atmos. **118**: 13463–13475. doi:10.1002/2013jd020389.

Gong, G. C. 2004. Absorption coefficients of colored dissolved organic matter in the surface waters of the East China Sea. Terr. Atmos. Ocean. Sci. **15**: 75–87.

Gordon, H. R. 2005. Normalized water-leaving radiance: Revisiting the influence of surface roughness. Appl. Opt. **44**: 241–248. doi:10.3319/Tao.2004.15.1.75(O).

Gordon, H. R., O. B. Brown, R. H. Evans, J. W. Brown, R. C. Smith, K. S. Baker, and D. K. Clark. 1988. A semianalytic radiance model of ocean color. J. Geophys. Res. Atmos. **93**: 10909–10924. doi:10.1029/JD093iD09p10909.

Gordon, H. R., and M. Wang. 1994. Retrieval of water-leaving radiance and aerosol optical-thickness over the oceans with SeaWiFS - a preliminary algorithm. Appl. Opt. **33**: 443–452. doi:10.1364/AO.33.000443.

Hoge, F. E., and P. E. Lyon. 1996. Satellite retrieval of inherent optical properties by linear matrix inversion of oceanic radiance models: An analysis of model and radiance measurement errors. J. Geophys. Res. Oceans **101**: 16631–16648. doi:10.1029/96JC01414.

Hu, C. 2009. A novel ocean color index to detect floating algae in the global oceans. Remote Sens. Environ. **113**: 2118–2129. doi:10.1016/j.rse.2009.05.012.

Hu, C., Z. Lee, and B. A. Franz. 2012. Chlorophyll a algorithms for oligotrophic oceans: A novel approach based on three-band reflectance difference. J. Geophys. Res. **117**: C01011. doi:10.1029/2011JC007395.

IOCCG. 2006. Remote sensing of inherent optical properties: Fundamentals, tests of algorithms, and applications. Lee, Z. (Ed.), Reports of International Ocean-Color Coordinating Group, No. 5, IOCCG, Dartmouth, Canada. doi:10.25607/OBP-96.

IOCCG. 2010. Atmospheric correction for remotely-sensed ocean-colour products. Wang, M. (Ed.), Reports of International Ocean-Color Coordinating Group, No. 10, IOCCG, Dartmouth, Canada. doi:10.25607/OBP-101.

Kostadinov, T. S., D. A. Siegel, and S. Maritorena. 2009. Retrieval of the particle size distribution from satellite ocean color observations. J. Geophys. Res. Oceans **114**: C09015. doi:10.1029/2009JC005303.

Lee, Z. P., K. L. Carder, and R. A. Arnone. 2002. Deriving inherent optical properties from water color: A multiband quasi-analytical algorithm for optically deep waters. Appl. Opt. **41**: 5755–5772. doi:10.1364/AO.41.005755.

Lee, Z. P., R. Arnone, C. M. Hu, P. J. Werdell, and B. Lubac. 2010. Uncertainties of optical parameters and their propagations in an analytical ocean color inversion algorithm. Appl. Opt. **49**: 369–381. doi:10.1364/Ao.49.000369.

Maritorena, S., D. A. Siegel, and A. R. Peterson. 2002. Optimization of a semianalytical ocean color model for global-scale applications. Appl. Opt. **41**: 2705–2714. doi:10.1364/AO.41.002705.

Mcclain, C. R. 2009. A decade of satellite ocean color observations. Ann. Rev. Mar. Sci. **1**: 19–42. doi:10.1146/annurev.marine.010908.163650.

Mcclain, C. R., G. C. Feldman, and S. B. Hooker. 2004. An overview of the SeaWiFS project and strategies for producing a climate research quality global ocean bio-optical time series. Deep-Sea Res. Part II Top. Stud. Oceanogr. **51**: 5–42. doi:10.1016/j.dsr2.2003.11.001.

Miller, R. L., and B. A. Mckee. 2004. Using MODIS Terra 250 m imagery to map concentrations of total suspended matter in coastal waters. Remote Sens. Environ. **93**: 259–266. doi:10.1016/j.rse.2004.07.012.

Milliman, J. D., and R. H. Meade. 1983. World-wide delivery of river sediment to the oceans. J. Geol. **91**: 1–21. doi:10.1086/628741.

Milliman, J. D., H. T. Shen, Z. S. Yang, and R. H. Meade. 1985. Transport and deposition of river sediment in the Changjiang Estuary and adjacent continental-shelf. Cont. Shelf Res. **4**: 37–45. doi:10.1016/0278-4343(85)90020-2.

Mobley, C. D., and others. 1993. Comparison of numerical-models for computing underwater light fields. Appl. Opt. **32**: 7484–7504. doi:10.1364/AO.32.007484.

Mobley, C. D., and L. K. Sundman. 2013. HydroLight 5.2 - EcoLight 5.2 users' guide. Sequoia Scientific.

Moreira, D., C. G. Simionato, F. Gohin, F. Cayocca, and M. L. C. Tejedor. 2013. Suspended matter mean distribution and seasonal cycle in the Rio de La Plata estuary and the adjacent shelf from ocean color satellite (MODIS) and in-situ observations. Cont. Shelf Res. **68**: 51–66. doi:10.1016/j.csr.2013.08.015.

Morel, A., and B. Gentili. 1996. Diffuse reflectance of oceanic waters. 3. Implication of bidirectionality for the remote-sensing problem. Appl. Opt. **35**: 4850–4862. doi:10.1364/AO.35.004850.

Morel, A., and S. Maritorena. 2001. Bio-optical properties of oceanic waters: A reappraisal. J. Geophys. Res. Oceans **106**: 7163–7180. doi:10.1029/2000JC000319.

Nechad, B., and others. 2015. CoastColour Round Robin data sets: A database to evaluate the performance of algorithms for the retrieval of water quality parameters in coastal waters. Earth Syst. Sci. Data **7**: 319–348. doi:10.5194/essd-7-319-2015.

O'Reilly, J. E., and others. 1998. Ocean color chlorophyll algorithms for SeaWiFS. J. Geophys. Res. Oceans **103**: 24937–24953. doi:10.1029/98JC02160.

Reynolds, R. A., D. Stramski, and B. G. Mitchell. 2001. A chlorophyll-dependent semianalytical reflectance model derived from field measurements of absorption and backscattering coefficients within the Southern Ocean. J. Geophys. Res. **106**: 7125–7138. doi:10.1029/1999JC000311.

Ruddick, K. G., V. De Cauwer, Y. J. Park, and G. Moore. 2006. Seaborne measurements of near infrared water-leaving reflectance: The similarity spectrum for turbid waters. Limnol. Oceanogr. **51**: 1167–1179. doi:10.4319/lo.2006.51.2.1167.

Shen, F., M. S. Salama, Y. X. Zhou, J. F. Li, Z. B. Su, and D. B. Kuang. 2010a. Remote-sensing reflectance characteristics of highly turbid estuarine waters - a comparative experiment of the Yangtze River and the Yellow River. Int. J. Remote Sens. **31**: 2639–2654. doi:10.1080/01431160903085610.

Shen, F., W. Verhoef, Y. X. Zhou, M. S. Salama, and X. L. Liu. 2010b. Satellite estimates of wide-range suspended sediment concentrations in Changjiang (Yangtze) Estuary using MERIS data. Estuaries Coast. **33**: 1420–1429. doi:10.1007/s12237-010-9313-2.

Shi, W., and M. Wang. 2009a. An assessment of the black ocean pixel assumption for MODIS SWIR bands. Remote Sens. Environ. **113**: 1587–1597. doi:10.1016/j.rse.2009.03.011.

Shi, W., and M. Wang. 2009b. Green macroalgae blooms in the Yellow Sea during the spring and summer of 2008. J. Geophys. Res. Oceans **114**: C12010. doi:10.1029/2009JC05513.

Shi, W., and M. Wang. 2009c. Satellite observations of flood-driven Mississippi River plume in the spring of 2008. Geophys. Res. Lett. **36**: L07607. doi:10.1029/2009GL037210.

Shi, W., and M. Wang. 2010. Characterization of global ocean turbidity from moderate resolution imaging spectroradiometer ocean color observations. J. Geophys. Res. Oceans **115**: C11022. doi:10.1029/2010JC006160.

Shi, W., and M. Wang. 2012. Satellite views of the Bohai Sea, Yellow Sea, and East China Sea. Prog. Oceanogr. **104**: 30–45. doi:10.1016/j.pocean.2012.05.001.

Shi, W., and M. Wang. 2014. Ocean reflectance spectra at the red, near-infrared, and shortwave infrared from highly turbid waters: A study in the Bohai Sea, Yellow Sea, and East China Sea. Limnol. Oceanogr. **59**: 427–444. doi:10.4319/lo.2014.59.2.0427.

Shi, W., and M. Wang. 2017. Characterization of particle backscattering of global highly turbid waters from VIIRS ocean color observations. J. Geophys. Res. Oceans **122**: 9255–9275. doi:10.1002/2017JC013191.

Shi, W., Y. Zhang, and M. Wang. 2018. Deriving total suspended matter concentration from the near-infrared-based inherent optical properties over turbid waters: A case study in Lake Taihu. Remote Sens. **10**: 333. doi:10.3390/rs10020333.

Shi, W., and M. Wang. 2019. Characterization of suspended particle size distribution in global highly turbid waters from VIIRS measurements. J. Geophys. Res. Oceans **124**. doi:10.1029/2018JC014793.

Son, S., and M. Wang. 2012. Water properties in Chesapeake Bay from MODIS-Aqua measurements. Remote Sens. Environ. **123**: 163–174. doi:10.1016/j.rse.2012.03.009.

Stramski, D., M. Babin, and S. B. Wozniak. 2007. Variations in the optical properties of terrigenous mineral-rich particulate matter suspended in seawater. Limnol. Oceanogr. **52**: 2418–2433. doi:10.4319/lo.2007.52.6.2418.

Tzortziou, M., and others. 2006. Bio-optics of the Chesapeake Bay from measurements and radiative transfer closure. Estuar. Coast. Shelf Sci. **68**: 348–362. doi:10.1016/j.ecss.2006.02.016.

Valente, A., and others. 2016. A compilation of global bio-optical in situ data for ocean-colour satellite applications. Earth Syst. Sci. Data **8**: 235–252. doi:10.5194/essd-8-235-2016.

Wang, M. 2006. Effects of ocean surface reflectance variation with solar elevation on normalized water-leaving radiance. Appl. Opt. **45**: 4122–4128. doi:10.1364/AO.45.004122.

Wang, M. 2007. Remote sensing of the ocean contributions from ultraviolet to near-infrared using the shortwave infrared bands: Simulations. Appl. Opt. **46**: 1535–1547. doi:10.1364/AO.46.001535.

Wang, M., and W. Shi. 2007. The NIR-SWIR combined atmospheric correction approach for MODIS ocean color data processing. Opt. Express **15**: 15722–15733. doi:10.1364/OE.15.015722.

Wang, M., S. Son, and L. W. Harding. 2009. Retrieval of diffuse attenuation coefficient in the Chesapeake Bay and turbid ocean regions for satellite ocean color applications. J. Geophys. Res. Oceans **114**: C10011. doi:10.1029/2009JC005286.

Wang, M., and others. 2013. Impacts of VIIRS SDR performance on ocean color products. J. Geophys. Res. Atmos. **118**: 10347–10360. doi:10.1002/jgrd.50793.

Wang, M., and others. 2014. Evaluation of VIIRS ocean color products. In: Proc. SPIE 9261, Ocean Remote Sensing and Monitoring from Space, Beijing, China. 92610E (10 December, 2014), doi:10.1117/12.2069251

Wang, M., W. Shi, L. D. Jiang, and K. Voss. 2016. NIR- and SWIR-based on-orbit vicarious calibrations for satellite ocean color sensors. Opt. Express **24**: 20437–20453. doi:10.1364/OE.24.020437.

Wang, M., and S. Son. 2016. VIIRS-derived chlorophyll-a using the ocean color index method. Remote Sens. Environ. **182**: 141–149. doi:10.1016/j.rse.2016.05.001.

Wang, M., and L. Jiang. 2018. VIIRS-derived ocean color product using the imaging bands. Remote Sens. Environ. **206**: 275–286. doi:10.1016/j.rse.2017.12.042.

Werdell, P. J., S. W. Bailey, B. A. Franz, L. W. Harding, G. C. Feldman, and C. R. Mcclain. 2009. Regional and seasonal variability of chlorophyll-a in Chesapeake Bay as observed by SeaWiFS and MODIS-Aqua. Remote Sens. Environ. **113**: 1319–1330. doi:10.1016/j.rse.2009.02.012.

Werdell, P. J., and others. 2013. Generalized ocean color inversion model for retrieving marine inherent optical properties. Appl. Opt. **52**: 2019–2037. doi:10.1364/AO.52.002019.

Wozniak, S. B., and D. Stramski. 2004. Modeling the optical properties of mineral particles suspended in seawater and their influence on ocean reflectance and chlorophyll estimation from remote sensing algorithms. Appl. Opt. **43**: 3489–3503. doi:10.1364/AO.43.003489.

Zhang, M., J. W. Tang, Q. Dong, Q. T. Song, and J. Ding. 2010a. Retrieval of total suspended matter concentration in the Yellow and East China Seas from MODIS imagery. Remote Sens. Environ. **114**: 392–403. doi:10.1016/j.rse.2009.09.016.

Zhang, M., J. Tang, Q. J. Song, and Q. Dong. 2010b. Backscattering ratio variation and its implications for studying particle composition: A case study in Yellow and East China Seas. J. Geophys. Res. Oceans **115**: C12014. doi:10.1029/2010JC006098.

Zhang, Y., X. H. Liu, Y. Yin, M. Z. Wang, and B. Q. Qin. 2012. A simple optical model to estimate diffuse attenuation coefficient of photosynthetically active radiation in an extremely turbid lake from surface reflectance. Opt. Express **20**: 20482–20493. doi:10.1364/OE.20.020482.

Acknowledgments

The VIIRS ocean color data imageries and calibration/validation results can be found at the NOAA Ocean Color Team website (https://www.star.nesdis.noaa.gov/sod/mecb/color/) and VIIRS mission-long ocean color data are freely available through the NOAA CoastWatch website (https://coastwatch.noaa.gov/). We thank two anonymous reviewers for their useful comments. The views, opinions, and findings contained in this article are those of the authors and should not be construed as an official NOAA or U.S. Government position, policy, or decision.

Conflict of Interest

None declared.

Submitted 04 October 2018
Revised 15 April 2019 and 06 May 2019
Accepted 09 May 2019

Associate editor: Xiao Hua Wang